C55.13/2: ERL ARL-110

NOAA Technical Memorandum ERL ARL-110

COMPLETED

50

STRATOSPHERIC LIDAR INVESTIGATIONS OF THE MT. ST. HELENS VOLCANIC CLOUD OVER BOULDER, COLORADO

John C. Osborn, Jr.
John J. DeLuisi
Ronald W. Fegley

Air Resources Laboratories
Silver Spring, Maryland
February 1982

noaa NATIONAL OCEANIC AND ATMOSPHERIC ADMINISTRATION / Environmental Research Laboratories

NOAA Technical Memorandum ERL ARL-110

STRATOSPHERIC LIDAR INVESTIGATIONS OF THE MT. ST. HELENS VOLCANIC CLOUD OVER BOULDER, COLORADO

John C. Osborn, Jr.
John J. DeLuisi
Ronald W. Fegley

Geophysical Monitoring for Climatic Change
Boulder, Colorado

Air Resources Laboratories
Silver Spring, Maryland
February 1982

UNITED STATES
DEPARTMENT OF COMMERCE
Malcolm Baldrige,
Secretary

NATIONAL OCEANIC AND
ATMOSPHERIC ADMINISTRATION
John V. Byrne,
Administrator

Environmental Research
Laboratories
George H. Ludwig
Director

I

NOTICE

Mention of a commercial company or product does not constitute an endorsement by NOAA Environmental Research Laboratories. Use for publicity or advertising purposes of information from this publication concerning proprietary products or the tests of such products is not authorized.

CONTENTS

	Page
ABSTRACT	1
I. INTRODUCTION	1
II. INSTRUMENTATION	2
III. DATA REDUCTION	2
IV. MEASUREMENT UNCERTAINTY SOURCES	9
V. DISCUSSION	12
ACKNOWLEDGMENTS	20
REFERENCES	21
APPENDIX	23

STRATOSPHERIC LIDAR INVESTIGATIONS OF THE MT. ST. HELENS VOLCANIC CLOUD OVER BOULDER, COLORADO

John C. Osborn, Jr., John J. DeLuisi, Ronald W. Fegley

ABSTRACT. Layered volcanic aerosol enhancement, after the Mt. St. Helens May 18, 1980, major eruption, was observed during May, June, and July 1980 over Boulder, Colo. A lidar system with dyelaser (λ = 590.0 nm) was the primary raw data acquisition source. Supplemental lidar return data from another source, were also used. Final data, presented as backscatter ratio versus altitude plots, were determined using the "molecular normalization" reduction method, which many previous literature works describe. Denver, Colo., NWS rawinsonde data were used to obtain the real molecular (Rayleigh) backscattering profiles needed for more accurate reduction. Potential error sources involved in collecting and final processing are discussed. Points of interest and discussion in the text include layering, vertical migration and temporal variability, layer classifications and characteristics changes, peak ratio intercomparisons, cloud trajectory and global transit time, eruption plume/satellite photograph intercomparison, and a simple determination of the ratio range of background stratospheric aerosol backscatter for comparison with the volcanically enhanced backscatter ratio data over Boulder.

I. INTRODUCTION

On May 18, 1980, Mt. St. Helens, a dormant volcano located in southwestern Washington State's Cascade range, violently erupted. Ejecta penetrated 10-11 km into the stratosphere, to a height of 22-23 km A.S.L. (Danielsen, 1981). This provided the continental United States with its first locally derived volcanic aerosol cloud since the 19th century.

Upper atmospheric aerosol distribution information has been previously shown and discussed using laser radar (lidar) measuring programs (Fiocco and Grams, 1964; Reiter and Carnuth, 1975; Russell and Hake, 1977; McCormick et al., 1978; Reiter et al., 1979). Russell et al. (1976) described a lidar measuring technique for observing aerosol backscattering layers and determining existence, extent, and variability.

During the 1980 late spring and early summer the GMCC stratospheric lidar program at Boulder was involved with final tests and training of new observatory personnel on the lidar system which was to be installed eventually at the Pt. Barrow, Alaska, baseline monitoring station. An observational test series was progressing at that time. Immediately after the May 18 eruption, so personnel training could be continued as well as data obtained, observations at regular intervals were undertaken. Between May 18 and July 29, 1980, 17 such observations show volcanically induced aerosol enhancement at various upper tropospheric and lower stratospheric levels over Boulder, Colo., and 6 show no enhancement. Five supplemental lidar observations, taken within the above time span and obtained from the NOAA Wave Propagation Laboratory, corroborate further the volcanic aerosol enhancement over Boulder that the GMCC 17-observation series details.

II. INSTRUMENTATION

During the 1980 late spring and early summer, the Boulder/Pt. Barrow lidar system was located at the east University of Colorado campus, NOAA/NCAR laboratory building, on the 7th floor. The room housing the system was equipped with a clear-glass zenith skylight. Table 1 presents pertinent lidar system electronic and instrumentation information; figure 1 gives the system block diagram and signal paths. The Phase-R dyelaser (λ = 590.0 nm) and its control high-voltage power supply can be fired manually, or with a photodiode trigger circuit through the CAMAC controlling module electronics (Computer Automated Measurement and Control, a standard modular instrumentation and digital interface system; Jay. 1977). The pulsed laser beam is projected at a zero-degree zenith angle. Radiation backscattered from atmospheric particulates or gases, as a function of height, is picked up by an EMI S-20 photomultipler, which can be made more sensitive, thus obtaining higher altitude resolution, by increasing the power supply voltage. Optimum adjustment can reduce or eliminate return signal saturation; our adjustments minimized saturation below 20 km above Boulder. The return signal is then sent through a gain switching amplifier which compensates for the rapid backscattered signal decrease with increasing altitude (Schuster, 1970) (Fox et al., 1973). The Biomation 805 waveform recorder accepts the amplified signal and performs an analog-to-digital conversion, that ensures total system compatibility. Finally, the system-compatible digital return data are transmitted through the CAMAC control module to a NOVA III minicomputer for eventual recording on Data General magnetic tape cassettes and on-line processing. Data output is obtainable by teletype, in a log total backscattering coefficient versus altitude format: The five supplemental NOAA/WPL lidar observations (λ = 694.3 nm), used to complete the Mt. St. Helens data set, were obtained as total backscattering coefficient versus altitude printouts.

III. DATA REDUCTION

The total backscattered energy return, divided by the expected purely molecular atmospheric return (Rayleigh backscattering) is the accepted lidar data presentation mode. It is referred to as the backscatter ratio. Russell et al. (1976) give the basic ratio computation relationships used as follows: The total measured range corrected lidar signal profile, at an altitude Z, is given by

$$S(Z) = K(f_m(Z) + f_p(Z))q^2(Z). \quad (1)$$

The computed molecular (Rayleigh) signal profile, at an altitude (Z), is given by

$$M(Z) = K(f_m(Z))q^2(Z). \quad (2)$$

Finally, the backscatter ratio, at an altitude Z, is given by

$$S(Z)/_{M(Z)} = f_m(Z) + f_p(Z) \; / f_m(Z). \quad (3)$$

Table 1. GMCC Boulder, Colo./Pt. Barrow, Alaska lidar system electronic and instrumentation information

Pulse energy	1.5 J
Pulse duration	0.6 ms
Pulse rate	30 pulses min^{-1}
Primary wavelength (variable)	590 nm
Peak power	2.5 mW
Receiver aperture (diameter) (plastic Fresnel lens)	40 cm
Photomultiplier	EMI S-20
Digitizer	Biomation 805

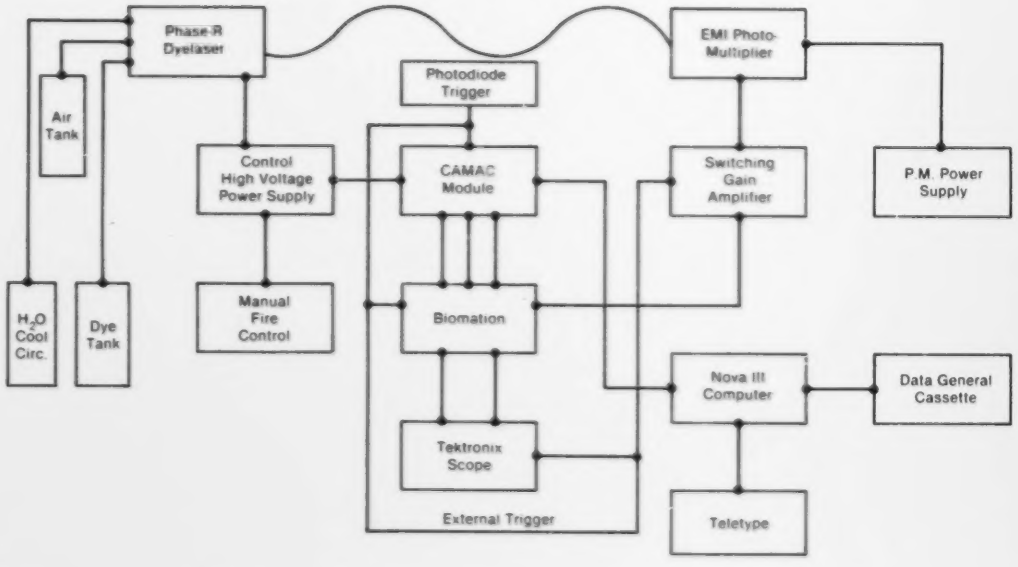

Figure 1.--GMCC Boulder, Colo./Pt. Barrow, Alaska, lidar system block diagram.

BEST DOCUMENT AVAILABLE

where

$f_m(Z)$ = Molecular (Rayleigh) backscattering coefficient at (Z);

$f_p(Z)$ = Particulate backscattering coefficient at (Z);

$q^2(Z)$ = Two-way optical transmission between (Z_1) and (Z), where (Z_1) is the lowest height at which the total return signal is analysed (the Boulder/Barrow system begins signal analysis at altitude = 0 km, but data from 0-5 km are disregarded);

K = System factor which includes

A. Total transmitted laser pulse energy.

B. Two-way transmission between the lidar and altitude Z_1.

C. Lidar calibration constant.

The lidar system minicomputer, with on-line processing, gives a log total backscattering coefficient ($f_m + f_p$) versus altitude teletype output. Schuster (1970) and Russell et al. (1976) discuss total backscattering data anomalies, because of the switching gain amplifier transients, at the corresponding altitude datum shifts where the gain switches occur. These few data anomalies were eliminated from consideration before final backscattering ratio processing.

Molecular (Rayleigh) backscattering coefficient profiles were computed using Denver, Colo., National Weather Service Forecast Center rawinsonde data provided by the National Center for Atmospheric Research (NCAR), Boulder, Colo., where the rawinsonde and lidar observation times corresponded as closely as possible. Russell et al. (1976) give the basic equation used:

$$f_m(Z) = N_m(Z) \times \sigma_m(Z) \times 10^2 \qquad (m^{-1}ster^{-1}), \tag{4}$$

where

$N_m(Z)$ = Molecular number density at (Z)(no. cm^{-3});

$\sigma_m(Z)$ = Rayleigh backscattering cross section of an air molecule, at the yellow dyelaser wavelength (λ=590.0 nm) at (Z) (cm^2ster^{-1}).

The number density is computed from the mass density which is obtained from the rawinsonde temperature and pressure at altitude Z and the equation of state, and a one-air-molecule mass value (4.8103×10^{-23}g) determined from a relationship given by Shortley and Williams (1971):

$$\text{No. molecules air} = Na \times N, \tag{5}$$

where

Na = Avogadros number = >6.0225×10^{23} molecules/mole.

n = Number of moles where one mole air = 28.97g.

Real mass density profiles, as determined from local rawinsonde data, are more accurate and timely than N.A.C.A. "Standard Atmosphere" derived mass density profiles, because local synoptic variations are taken into account. Denver rawinsonde data and "Standard Atmosphere" data can show fairly large deviations.

McCartney (1976) gives an expression for calculating a Rayleigh angular scattering cross section:

$$\sigma_m(\Phi) = \pi^2(n_a^2-1)^2/N_m^2\lambda^4 \quad \sin^2\Phi \quad (cm^2 ster^{-1}), \tag{6}$$

where

Φ = Angle between a model molecular scatterer's oscillating dipole moment axis and any direction of interest. For backscattering, $\Phi = 90^o$; thus $\sin^2\phi = 1$.

N_m = Molecular number density previously determined.

λ = Wavelength (590.0 nm-yellow dyelaser).

n_a = Refractive index of air, computed from the rawinsonde temperature, pressure, and moisture data at (Z), wavelength, and a simplified expression

version, given by Kneizys et al. (1980), from Edlen (1966);

$$(n_a - 1)\ 10^6 = \left(77.46 + \frac{0.459}{\lambda^2}\right)\frac{P}{T} - \frac{p_{H_2O}}{1013.25}\left(43.49 - \frac{0.347}{\lambda^2}\right), \tag{7}$$

where

P = Atmospheric pressure (mb).

T = Ambient temperature (K).

pH_2O = Partial water vapor pressure (mb).

Log total and log molecular (Rayleigh) backscattering coefficient curves that have equivalent altitude scales were generated. Figure 2 shows a log total backscattering coefficient versus altitude curve example, using 5-19-80, 0757Z, lidar return data. Note the volcanic-aerosol-induced curve perturbations at 8 and 13 km above Boulder, and the smooth curve minimum just below the 8 km perturbation. Table 2 gives molecular (Rayleigh) backscattering coefficient, altitude, and related computations, using the 5-19-80, 1200Z, Denver rawinsonde temperature, pressure, and moisture data, plus the equations and information previously listed and discussed. Figure 3 presents Table 2's log molecular (Rayleigh) backscattering coefficient versus altitude data graphically. Notice the gradual decrease with increasing altitude because of the decreasing molecular number density, as Table 2 reveals. The altitudes listed above the abscissa in figs. 2 and 3 are those at which the amplifier gain switches occur; thus the corresponding altitude datum shifts. A real atmosphere total backscattering coefficient profile, and the calculated molecular (Rayleigh) backscattering coefficient profile component have similar general curve shapes. The addition of a volcanic particulate backscattering coefficient profile component and the calculated molecular (Rayleigh) backscattering coefficient component, however, should give the real atmospheric backscattering profile.

The difference between the total and molecular (Rayleigh) curves, at this processing stage, is an indirect measure of K, the system factor, which cannot be directly determined, because the Boulder/Barrow lidar system has no absolute sensitivity calibration provision. Final ratio processing eliminates the indirect system factor from consideration by adopting the "matching" "clean-air calibration," or "molecular normalization," reduction method, previously used and discussed in many varying lidar measurement programs (Fiocco and Grams, 1964; Grams and Fiocco, 1967; Schuster, 1970; Russel et al., 1976; Russell and Hake, 1977; Itabe et al., 1977; McCormick et al., 1978; Reiter et al., 1979). The basic assumption is that at some level within the complete lidar profile range there are no particulates and thus no total backscattering particulate contribution; at this level the total backscattering coefficient equals the molecular (Rayleigh), and the backscatter ratio is unity. We further assume that this specific level is represented by a log total backscattering coefficient versus altitude curve smooth minima region, which is near to the total curve perturbations caused by volcanic aerosol backscattered energy contributions. Figure 2's previously mentioned 5-6.48 km altitude range is a prime example. The molecular (Rayleigh) log backscattering coefficient curve is then fitted, along the corresponding altitude axes, to the total curve smooth minima (Fiocco and Grams, 1964). The difference between the two curves now represents the volcanic aerosol backscattering contribution, and layer height, intensity, and temporal variation information can be obtained.

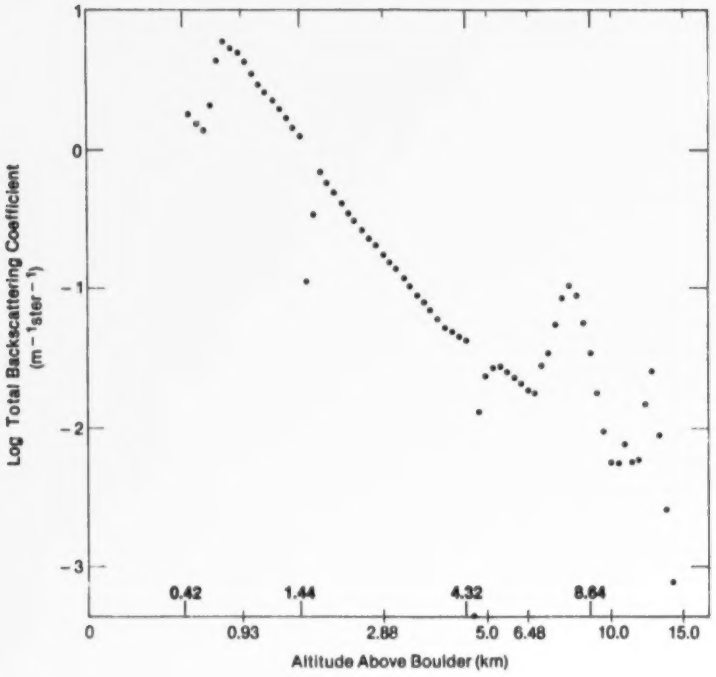

Figure 2.--Log total backscattering coefficient profile, 5-19-80, 0757Z.

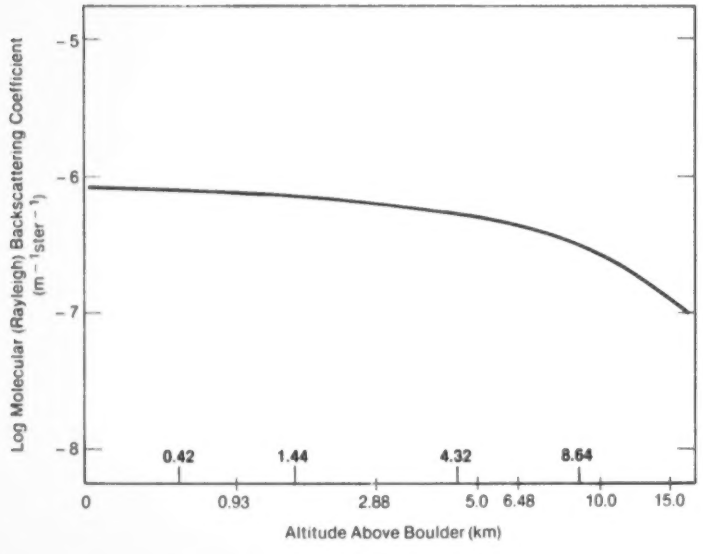

Figure 3.--Log molecular (Rayleigh) backscattering coefficient profile (5-19-80, 1200Z rawinsonde, for 5-19-80, 0757Z lidar observation).

BEST DOCUMENT AVAILABLE

Table 2. Rawinsonde and calculated data inputs for molecular (Rayleigh) backscattering coefficient versus altitude computations (5-19-80, 1200Z rawinsonde for 5-19-80, 0757Z lidar observation)

Altitude Above Boulder-Rwsonde & Hydrostatic Eq. (km)	Mass Density Rawinsonde & Eq. of State ($gcm^{-3}x10^{-3}$)	No. Density 1 Molecule $\frac{4.8103x10^{-23}g}{}$ (No. $cm^{-3}x10^{19}$)	Refractive Index of air + λ=590 nm, Kneizys et al., 1980, from Edlen, 1966 ($x10^{-4}$ + 1.0)	Rayleigh Bscat. Cross Section McCartney, 1976 ($cm^2ster^{-1}x10^{-28}$)	Molecular (Rayleigh) Bscat. Coef. Russell et al., 1976 ($m^{-1}ster^{-1}x10^{-7}$)	Log Molecular (Rayleigh) Bscat. Coef.
0	1.043	2.168	2.36	3.861	8.372	-6.077
.54	.979	2.036	2.20	3.806	7.748	-6.111
.93	.932	1.938	2.11	3.863	7.487	-6.126
1.50	.885	1.841	2.00	3.847	7.081	-6.150
2.14	.834	1.732	1.89	3.878	6.719	-6.173
2.71	.775	1.612	1.79	4.020	6.478	-6.189
3.56	.726	1.509	1.64	3.851	5.810	-6.236
4.11	.683	1.420	1.54	3.835	5.444	-6.264
5.22	.605	1.257	1.37	3.872	4.866	-6.313
6.10	.553	1.149	1.25	3.859	4.432	-6.353
7.01	.498	1.034	1.14	3.958	4 094	-6.388
7.72	.455	.947	1.03	3.859	3.652	-6.437
8.92	.395	.822	.89	3.823	3.141	-6.503
9.48	.366	.760	.83	3.884	2.953	-6.530
10.34	.320	.665	.72	3.825	2.542	-6.595
11.19	.282	.586	.62	3.645	2.137	-6.670
12.19	.241	.500	.54	3.798	1.900	-6.721
14.33	.174	.362	.39	3.822	1.385	-6.858
14.76	.162	.336	.37	3.946	1.327	-6.877
16.40	.126	.261	.28	3.741	.978	-7.010

BEST DOCUMENT AVAILABLE

The normalization altitude value is of some importance. Itabe et al. (1977) give the optimum altitudes as either less than 15 km or more than 25 km A.S.L. The greater than 25-km backscattered energy return is very weak, which presents greater photon counting error possibilities (Itabe et al., 1977). Thus the 15-km region is the favored normalization altitude. We have varied each individual observation normalization height so that it corresponds to the log total backscattering coefficient versus altitude curve smooth minima previously discussed. This eliminates any backscatter ratios less than unity. However, our 22-observation series mean normalization height is 15.8 km. A.S.L. Reiter et al. (1979), using lidar observations over Germany from October 1976 to June 1978 give 14.4 km A.S.L. as the mean normalization altitude. If the normalization altitude chosen is not completely aerosol free, and the total measured backscattering coefficient does not equal the calculated molecular (Rayleigh) value at this altitude, the "matching", "clean air calibration" or "molecular normalization" reduction methods aerosol backscattering contribution determination will be below that which actually exists. There is no easy and direct aerosol-free level detection technique; thus our assumption that the total backscattering versus altitude curve smooth minima region previously discussed actually represents this desired aerosol-free altitude.

The final processing step eliminates the log factor by raising 10 to the power of the numerical difference between the two curves, after the normalization procedure. The final data product form is in terms of backscatter ratio versus altitude. The 17 GMCC and 5 supplemental NOAA/WPL lidar observations were analyzed, and are presented in this way. Figures A-1 through A-22, in the appendix, present the total 22-observation series backscatter ratio versus altitude data, plus corresponding rawinsonde wind, temperature, dewpoint, and pressure profiles. Many observations are indicative of special features that warrant a more detailed discussion, which will be forthcoming in a later text section.

IV. MEASUREMENT UNCERTAINTY SOURCES

Figure 4 presents percent error plots versus altitude A.S.L., for the possible error sources, using the Reiter et al. (1979) data set, with the 14.4-km A.S.L. mean normalization altitude previously mentioned. There are five potential error sources that can affect lidar measurement precision, as discussed by Reiter et al. (1979):

1.) Photon count statistical error. This is a function of the total photon count. Curve A, fig. 4, gives the Reiter et al. (1979) calculated 1σ mean-squared errors plotted versus altitude A.S.L. Neutral density filters, which reduce incoming intensity and allow single photon pulse resolution, have been placed in front of the photomultiplier tube, and cause the curves step pattern at 14 and 18 km A.S.L. The Boulder/Barrow lidar's photomultiplier and filter setup is similar to this, except for the neutral density filter's intensity reduction. Curve A., however, can also roughly represent the Mt. St. Helens volcanic cloud lidar measurements possible photon count statistical error.

2.) Alignment error. This results from intensity shifts in the received backscattered signal from the return profile's individual gate sections as caused by cirrus-induced tropospheric transmission alterations, and the gate sections realignment to give a valid total backscattering profile.

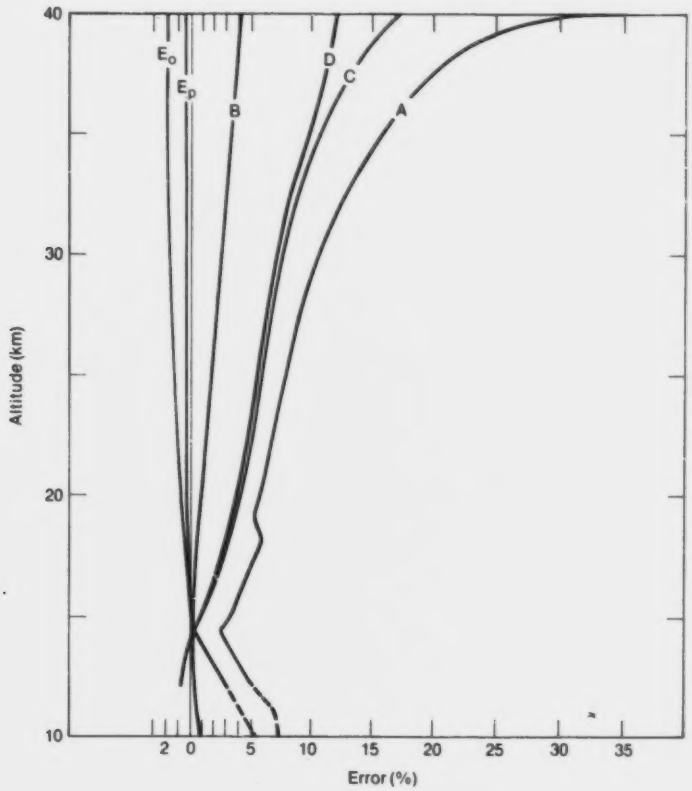

Figure 4.--Estimate of the errors involved in backscatter ratio determination (Reiter et al., 1979).

Curve B, fig. 4 shows the Reiter et al. (1979) derived percent alignment error at given altitudes. This error is maximized at the upper altitudes because more individual sections are required for a complete backscattering profile construction, and approaches zero as the altitude approaches the normalization level. The Mt. St. Helens lidar data set presented minimizes this potential error source two ways: a) not looking at return signals more than 20 km above Boulder, b) normalizing total backscattering profiles at levels very near the volcanically induced return data peaks. Thus, the section alignment induced error is zero at or near the backscatter ratio peaks, and approximately 1% at the 20-km upper bound.

3.) Rawinsonde uncertainty error in the temperature and pressure deduced density profile, which is used for the molecular (Rayleigh) backscattering versus altitude computations. Lenhard (1973) 1.5 mb and 0.1 mb pressure step data have been interpolated to 0.5 mb by Reiter, and are presented in curve C, fig. 4. This possible error source is kept at a minimum (less than 4%) by dealing only with data return from less than 20 km above Boulder.

4.) Real/Standard air density error. This is a meteorologically related error, introduced if the standard N.A.C.A. atmospheric pressure and temperature data are used for density calculations and molecular (Rayleigh) backscattering profile determination, as opposed to local rawinsonde-obtained information. This error can be pronounced over the Colorado front range, because local

BEST DOCUMENT AVAILABLE

pressure and temperature sounding data and the N.A.C.A. standard profile can differ dramatically. Curve D, fig. 4, presents the Reiter et al. (1979) percentage error versus altitude determination. Because the complete Mt. St. Helens lidar data set reduction process uses Denver rawinsonde data for molecular (Rayleigh) backscattering profile computations, as previously discussed, the real/standard air density error is not introduced.

5.) Particulate and ozone absorption derived two-way transmission variation error in the molecular (Rayleigh) backscattering profile calculation. The particulate and ozone atmospheric extinction coefficient contributions cause this error. Curve E, fig. 4, gives the Reiter et al. (1979) derived total error contributions, using mean annual ozone and particulate backscattering coefficient profiles (Eo = ozone error curve, Ep = particulate error curve). The error curves may not be entirely precise when applied to the complete Mt. St. Helens lidar data set, since mean ozone profiles differ and our particulate backscattering profiles are volcanically enhanced, and thus cannot be classified as an accurate mean annual particulate backscattering representation. For simplification purposes, however, the ozone and particulate error curves that fig. 4 presents have been accepted as representative. They are very small, reaching no higher than 1.5 percent at 20 km above Boulder, and zero at the 14.4 km A.S.L. mean normalization height. Further, they negate minute portions of the other four possible error sources, as fig. 4's six curves reveal. The ozone and particulate total extinction error contribution data curves are unbalanced with respect to the other possible errors, and result from atmospheric constituent transmission reduction underestimation when calculating the molecular (Rayleigh) backscattered energy return (Reiter et al., 1979). The potential thus exists for an even greater particulate extinction error contribution, further curve unbalancing, and more extensive negation of the other four possible error sources previously discussed, because during the combined lidar measurements over Boulder, the aerosol regime was heavily laden with volcanic particulates.

Reiter et al. (1979) gives a 10 percent backscatter ratio maximum total error allowable in order that short-term stratospheric aerosol layer variation descriptions may be meaningful. If the total measured backscattering equals the calculated molecular (Rayleigh) value at the normalization height chosen, as is the basic data reduction assumption used with the combined Mt. St. Helens set, fig. 4's curve summation represents the maximum total error when a backscatter ratio at a given altitude is determined (Reiter et al., 1979). When we take into account the curve D elimination altogether, lidar system differences and their quantitative effects on the five remaining error curves, the similar mean normalization heights, processing and examining return data only from less than 20 km above Boulder, and the mean annual ozone and particulate profile differences, the combined Mt. St. Helens lidar data set maximum total error falls below the 10 percent figure previously mentioned. At 20 km above Boulder (21.6 km A.S.L.) the maximum total backscatter ratio error range is 9%-10%, its greatest value over the altitude range we are most interested in. This error range drops with decreasing altitude, to 3%-4% at the Mt. St. Helens data sets 15.8 km A.S.L. mean normalization height. The range then slowly increases with further descent, to 8%-9% at roughly 12 km A.S.L., the error data limits. No error information is available below this altitude; thus, we will assume it falls below the 10 percent figure previously mentioned. Because the error range falls below the 10 percent figure previously mentioned throughout a fairly wide altitude span, we can present meaningful short-term volcanic aerosol layer intrusion information.

V. DISCUSSION

Sequential examination of figs. A-1 through A-22 reveals the layering of volcanic aerosol clouds, their vertical extent and migration, intensity, and temporal variability. Fernald and Frush (1975), and Russell and Hake (1977), give primary descriptive features for a volcanic aerosol cloud: 1) largest effects at altitudes below 20 km, 2) a multilayered structure early on, 3) giving way to one broad, less intense backscattering peak. The 22 observation series presented here reveals all three features.

Volcanic aerosol profile stratification and time variation, up to a 40-km A.S.L. altitude, was discussed by Schuster (1970). Three layer classifications are examined: I.) short-lived (less than 4 seconds) layers with spacing and thickness as little as 30 meters throughout the 40 km A.S.L. altitude range; II.) a well-defined layer (or layers), lasting several hours, near the tropopause; III.) the 18-22 km A.S.L. altitude "Junge" layer (Junge et al., 1961) subject to height and thickness variations. Our particular instrument setup, sensitivity, shot averaging, and data analysis method preclude the possibility of obtaining accurate information on such thin, short-lived layers as classification I describes. Holton (1972) gives a 12.7-13.0 km A.S.L. mean tropopause height range, at Boulder's latitude, during the summer. The combined lidar observation series we present shows pronounced backscattering layers at, or near, this height range, particularly figs. A-1 to A-3, A-7 to A-11, and A-14 to A-16. The Boulder/Barrow lidar system maximum altitude range is approximately 22 km A.S.L. so interpretation of this region's return data is difficult. However, figs. A-3 to A-6, A-12, A-13, A-16, A-17, and A-19 to A-22 are believed representative of the "Junge" stratospheric aerosol layer (Junge et al., 1961), as classification III described. They, too, show backscattering temporal variability and vertical migration, throughout the 18-22 km A.S.L. altitude range.

Russell and Hake (1977) discuss stratospheric aerosol layer day-to-day changing characteristics. First, after regular intensity decline during the first several detection days, the changes become small to negligible, indicating broad backscattering layer stability versus the more drastic intensity and layer height shifts during the first several detection days. This represents an unstable, highly variable, multilayered aerosol cloud quality as opposed to the stable single primary layer quality seen later on. Second, the greater backscattered energy intensity reductions with time at the lower versus higher altitudes is consistent with more effective aerosol removal processes at the lower altitudes. A prime process is particle sedimentation. The mean size distribution at 14-18 km A.S.L. is larger than at the higher altitudes, which implies more particle precipitation at the lower altitude range, and thus a reduced backscattered energy intensity and ratio reduction with time, over and above that measured at the 18-22 km A.S.L. "Junge" layer height (Junge et al., 1961).

The combined Mt. St. Helens lidar observation backscatter ratio profile series presented (figs. A-1 to A-22) exhibits both characteristic changes previously discussed. Figures A-1 through A-4 show lower altitude backscattered energy intensity reduction with time, as caused by cloud transit and large particle fallout. However, most observations, after this initial 4-day period, show gradual stabilization into one primary layer at 18-22 km A.S.L., particularly the late June and July observations (figs. A-17 through A-22). The backscattered intensity then can slowly diminish with slow volcanic stratospheric aerosol removal, because an effective cleansing process, like large-particle precipitation at lower levels, is not present above 17 km A.S.L. (Hofmann et al., 1975; Fernald and Frush, 1975).

Large backscatter ratios, where the particulate backscattering contribution is sometimes greater than 20 times the molecular (Rayleigh) contribution, can be detected from lidar observations (Fegley and Ellis, 1975; Fujiwara et al., 1975). Such ratios are indicative of extreme aerosol layer loading. A 24.24 maximum backscatter ratio was observed over Mauna Loa, Hawaii, just above the tropopause ($\cong$ 16 km. A.S.L.), after the October 1974 Volcán de Fuego eruption, using a ruby laser lidar system (λ = 694.3 nm). Fifteen hours later, the peak ratio was 1.64. Assuming no molecular (Rayleigh) backscattering component change, the ratio drop represents a 97% volcanic aerosol backscattering component decrease. The Boulder combined-observation series taken on the Mt. St. Helens volcanic cloud overpass gives a 29.72 peak backscatter ratio, at 17.5 km. A.S.L., and this is shown in fig. A-3. At the same altitude, 24 hours later, as seen in fig. A-4, the ratio was 7.10, but the peak backscatter ratio was at a different altitude. Again, assuming no molecular (Rayleigh) backscattering component change, this ratio drop indicates a 79% volcanic aerosol backscattering component decrease. These two examples illustrate a recently created volcanic aerosol cloud's highly transient nature and wide temporal variability. The layer peak backscatter ratio difference, between figs. A-3 and A-4, reveals a 0.5 km upward vertical migration.

Though the two peak ratios previously discussed cannot be directly compared, because the respective lidar system's laser wavelengths are different, the precedent is now established for these volcanic aerosol induced ratio magnitudes. Russell et al. (1976) discuss the backscatter ratio differences obtained from sequential lidar observations using first the ruby (λ = 694.3 nm), then the dye (λ = 590.0 nm) laser. The dyelaser profile ratios are smaller than the ruby profile values, because the molecular (Rayleigh) backscattering coefficients ratios contribution is λ^{-4} dependent. Further, the particulate backscattering coefficients ratio contribution is λ dependent, although less so than the molecular (Rayleigh).

Observed peak backscatter ratios of the Volcán de Fuego and Mt. St. Helens volcanic clouds are essentially the same magnitude, but the Fuego profiles were for λ = 694.3 nm, whereas Mt. St. Helens profiles were for λ = 590.0 nm. It could be inferred that the St. Helens cloud might have been more intense if the molecular (Rayleigh) backscattering coefficient's λ^{-4} dependence is the only consideration. However, the Guatemala-Mauna Loa distance and air mass trajectories were vastly different from the southwestern Washington-Boulder distance and trajectories. Danielsen (1981) gives May 19-22, 1980, constant pressure level trajectories, initialized at the Mt. St. Helens latitude and longitude, and covering a 300 to 100 mb height range over the western United States. Figure 5 presents the paths traveled starting eastward to the Washington-Idaho border, then turning southeast over Utah and Wyoming, covering Colorado, and on to Oklahoma and north Texas before turning eastward again. These paths, at the heights given, put the volcanic aerosol cloud maximum directly over Colorado. However, compared with the Mt. St. Helens volcanic cloud over Boulder, the Volcán de Fuego aerosol cloud over Mauna Loa underwent a more indirect global trajectory and longer transit time, while maintaining roughly the same magnitude backscatter ratio as seen from the Mt. St. Helens cloud over Boulder. This implies that the Fuego volcano produced a more intense eruption, with greater particulate intrusion and longer residence time, thus explaining the high backscatter ratio maintenance after the Guatemala-Mauna Loa three-fourths global transit, versus the southwestern Washington-Boulder 1200-mile cloud paths.

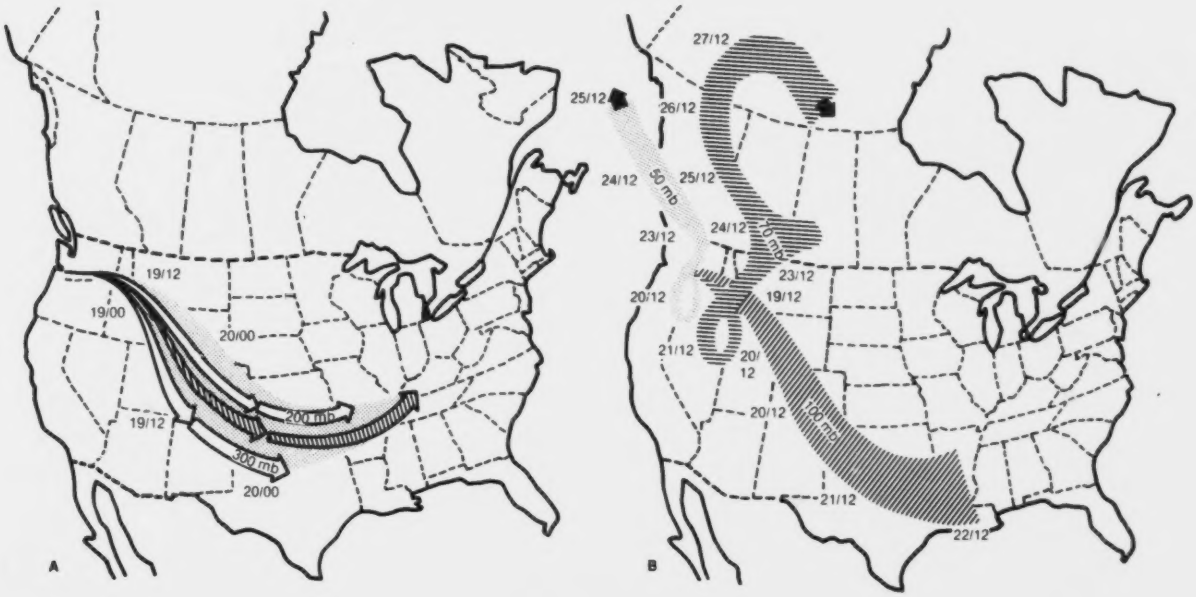

Figure 5.--(A) Upper tropospheric/lower stratospheric trajectories for 18 May eruption. (B) Lower mid-stratospheric trajectories for 18 May eruption. Date/time (hour) denotes day of month (May)/G.M.T. (Danielsen, 1981).

BEST DOCUMENT AVAILABLE

Volcanic aerosol cloud movement, plume shape, and characteristic changes during its Western United States transit, previously detailed, and displayed in fig. 5, are also discussed by Danielsen (1981). Heavy upper tropospheric/lower stratospheric ash loading and increased water content allow volcanic aerosol plume detection with satellite photographs, which also reveal the clouds' temporal variation. An erupting volcano's emission resembles an industrial stack effluence plume, flowing horizontally and increasing in diameter (Danielsen, 1981). The aerosol cloud turned southeast, as fig. 5 depicts, 24-30 hours after the eruption. Isentropic trajectories computed show that at this transit stage the volcanic cloud was descending (Danielsen, 1981). Eventually a 10.2 km A.S.L. low point was reached over Oklahoma, down from 12.8 km A.S.L. over Wyoming. This descending air was warmed by compression, with the water being evaporated and the satellite photograph appearance of the plume becoming a very thin white veil (Danielsen, 1981). Figures 6, 7, and 8 are satellite photographs taken by the GOES-West spacecraft, and obtained from NOAA, National Environmental Satellite Service, Washington, D.C. The photograph times are 6 minutes, 1 hour 6 minutes, and 2 hours 6 minutes after the eruption and sequentially they reveal the east-west and north-south volcanic cloud spreading, similar to a stack emission plume. The dark appearance indicates the extensive water content increase and ash loading, and only 2 hours 6 minutes after eruption the aerosol cloud covers roughly one-fourth of the states' area. Figure 9, also from NOAA/NESS GOES-West spacecraft, was taken 24 hours 6 minutes after the primary eruption, during the cloud's compression-warmed descent and water content evaporation. The very thin, white veilish appearance is revealed over central Montana and Wyoming, eastern Colorado, northwest Nebraska, and South Dakota's southwestern tip. Figure 9's time, 19 May 1980, 1545Z, falls between the times of lidar observations depicted in figs. A-1 and A-2. The volcanic aerosol cloud's multilayered structure is not apparent from the satellite photograph. All that can be seen is the upper portion, at 14.6 km A.S.L. However, fig. A-1's backscatter ratio profile reveals the multilayered structure. Figures A-1 and A-2 also document the cloud's descending motion over Colorado. The aerosol layer peaks have descended roughly 3 km, and fig. A-2's backscatter ratio profile is even more multilayered than fig. A-1's. It is this descending motion that causes the volcanic aerosol clouds dark gray to veilish white satellite photo appearance change. The change is due to water content evaporation, as the transition between fig. 8 and fig. 9 reveals.

Finally, Danielsen (1981) gives an approximately 15-day global transit time for the volcanic aerosol clouds upper tropospheric portion, between 200 and 150 mb. Two of the five lidar observations in which no volcanic aerosol backscatter was observed were taken on May 28 and 29, between figs. A-6 and A-7 observation times. Figure A-7, however, shows a lower, more intense backscattering layer at 13.7 km A.S.L. (170 mb) than can be seen at the same altitude in fig. A-6. This is just under 16 days after the cloud was first seen over Boulder (fig. A-1). Figure A-7's primary layer is the beginning of the somewhat diminished, but clearly existent volcanic aerosol cloud's second global transit.

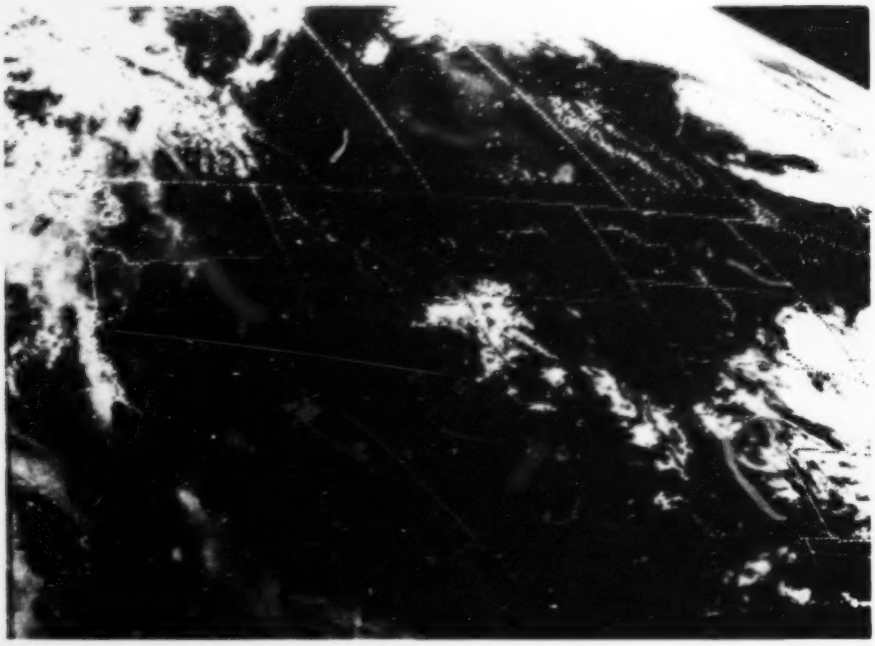

Figure 6.--Mt. St. Helens volcanic plume, 18 May 1980, 1545Z, 6 minutes after the major eruption, as seen from NOAA/NESS GOES-West spacecraft.

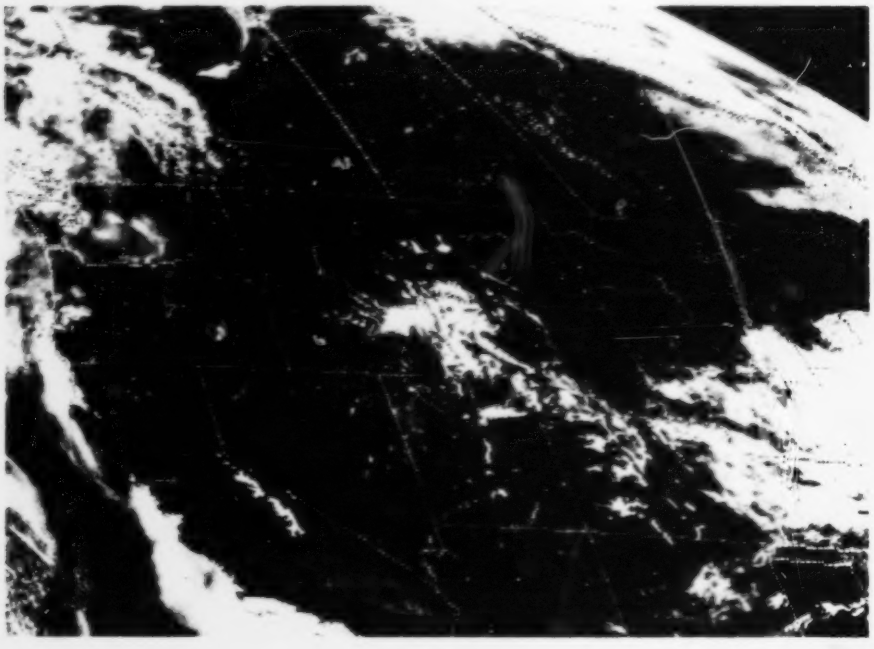

Figure 7.--Mt. St. Helens volcanic plume, 18 May 1980, 1645Z, 1 hour 6 minutes after the major eruption, as seen from NOAA/NESS GOES-West spacecraft.

BEST DOCUMENT AVAILABLE

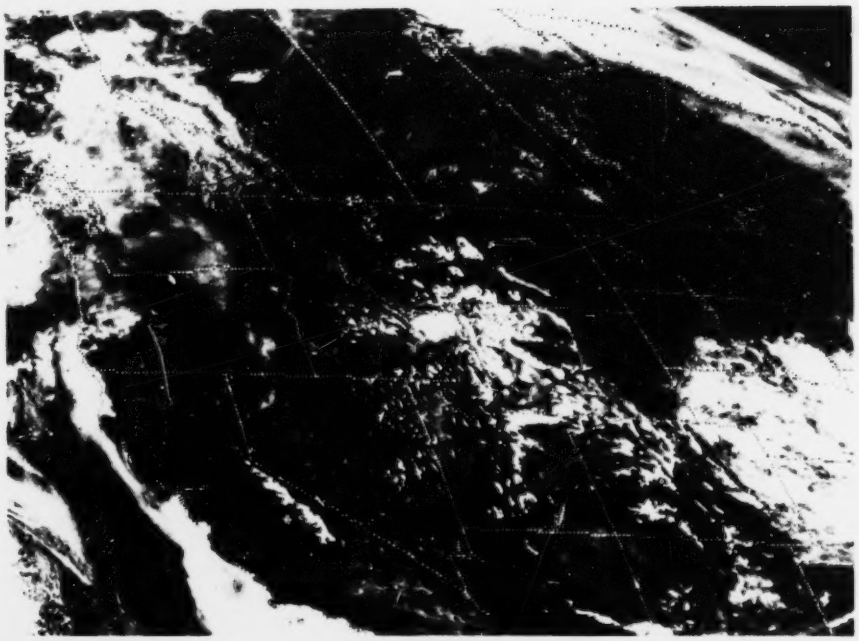

Figure 8.--Mt. St. Helens volcanic plume, 18 May 1980, 1745Z, 2 hours 6 minutes after the major eruption, as seen from NOAA/NESS GOES-West spacecraft.

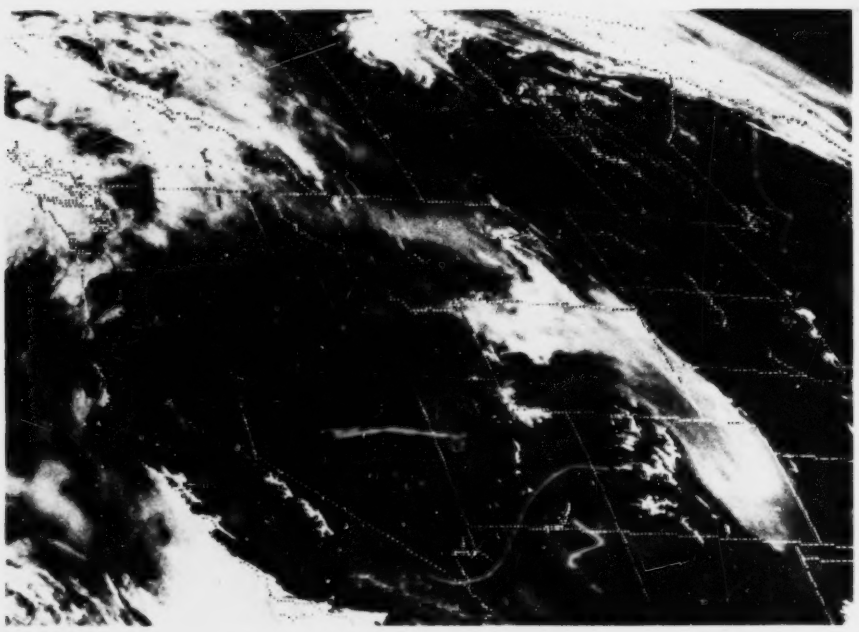

Figure 9.--Mt. St. Helens volcanic plume, 19 May 1980, 1545Z, 24 hours 6 minutes after the major eruption, as seen from NOAA/NESS GOES-West spacecraft.

BEST DOCUMENT AVAILABLE

Russell et al. (1976) give a 1.08-1.19 maximum backscatter ratio range, during the volcanically quiet time period 11/72-3/74, centered at the 18-22 km A.S.L. "Junge" layer (Junge et al., 1961) and obtained with a lidar system using a ruby laser (λ = 694.3 nm). Further, Hofmann and Rosen (1981) give an approximately 9% per year background stratospheric aerosol level increase at this same 18-22 km A.S.L. region. We now assume that this backscatter ratio range, during the quiet period, a stratospheric aerosol loading low point (McCormick et al., 1978), indicates background stratospheric aerosol conditions, with no drastic molecular (Rayleigh) backscattering contribution changes. Volcanic stratospheric aerosol enhancement, such as the fall 1974 Fuego eruption or the spring 1979 St. Vincent Island La Soufriére eruption, accounts for this 9% per year background level increase. The stratospheric aerosol source is thought by Hofmann et al. (1976) to be related to emanating tropospheric sulfurous gases, either quasi-statically or sporadically, as with volcanic eruptions. They discount the nonvolcanic, quasi-static tropospheric sulfurous aerosol source because of sulfur budget and model work considerations. It is a reasonably valid assumption, however, that most volcanic activity, except Volcán de Fuego, between 1974 and 1980, had minimal background stratospheric aerosol layer influence between 18 and 22 km A.S.L., other than the primary contribution to the 9% per year increase previously mentioned. The La Soufriére eruption had no 20 km A.S.L. stratospheric aerosol layer effect at northern middle latitudes (Rosen and Hofmann, 1980). The aerosol increase over Boulder induced by Alaska's Mt. Augustine eruption (Cadle et al., 1977), did not even attain a Fuego dust decay curve extrapolated aerosol level (Iwasaka, 1981), making its global scale stratospheric aerosol layer influence suspect. However, the Volcán de Fuego plume penetrated into the stratosphere with effects noted at many Northern Hemisphere locations during the cloud's global transport (Fegley and Ellis, 1975; Volz, 1975; Russell and Hake, 1977). But Hofmann and Rosen (1981) show that the early 1974 pre-Fuego maximum aerosol mixing ratio values (particles/mg air) were nearly reestablished by early 1978; the inexact reestablishment is probably indicating the 9% per year background increase previously discussed. Further, Hofmann et al. (1976) and Hofmann and Rosen (1981) give a constant background aerosol size distribution between the tropopause and approximately 25 km A.S.L. with a sulfur-predominating elemental composition. These constraints can imply that the backscatter ratios returned to roughly the background value range (1.08-1.19) previously stated, but reflecting also the 9% per year particulate increase, if there are no appreciable molecular density profile changes seen. The 9% per year background stratospheric aerosol level increase between 1974 and 1980, applied year to year to the total backscattered intensities aerosol contribution, using the size distribution and elemental composition criteria previously discussed, assuming no extreme molecular density profile variations, and if stated as a backscatter ratio range change, corresponds to a 4.4% total background backscatter ratio boundary increase during the same time period. The new ratio range of 1.13-1.24 roughly indicates background stratospheric aerosol conditions at the 18-22 km A.S.L. level just prior to the Mt. St. Helens eruption.

When the background backscatter ratio range criteria previously discussed are used, if we see lidar observation ratios in this range or below, at the 18-22 km A.S.L. "Junge" layer height (Junge et al., 1961), we would expect them to represent background stratospheric aerosol and not short-term enhancement above and beyond the 9% annual increase's volcanic contribution. However, over Boulder, Colo. the background condition is not the case. Figure A-19 shows an aerosol peak at 21-22 km A.S.L., with a 1.5 maximum backscatter ratio. Figure A-20, 1 hour later, gives an aerosol peak at the same height, with a 4.0 maximum backscatter ratio. (Figures A-21 and A-22, 1 day and 2 weeks later respectively, also show peaks at this height, with backscatter ratios above what could be considered background values.) Thus, it is believed that two months after the main eruption we still saw sporadic, but fairly extensive stratospheric aerosol volcanic contributions over Boulder, Colo., and not background conditions, within the previously mentioned assumptions constraints. The aerosol layer remained identifiable for months after the eruption, while it was slowly being dispersed by horizontal shears, small-scale turbulent motions (Danielsen, 1981), and particle precipitation. Our record is not long enough, however, and lidar data over short time periods should be carefully examined, because seasonal variation existence has been shown (McCormick et al., 1978), particularly below 22 km A.S.L. at northern middle-latitude locations (Hofmann et al., 1975). This would appear to corroborate the preliminary data of Hofmann and Rosen (1981) in revealing the stratospheric aerosol enhancement caused by the Mt. St. Helens volcanic eruption.

ACKNOWLEDGMENTS

This work was supported wholly by NOAA, Air Resources Laboratory, Geophysical Monitoring for Climatic Change Program. The authors extend best wishes and many thanks to the following individuals: G. McNice and T. Ketterman, WPL/ Optical Sensor Groups, for discussions and supplemental lidar return data; P. Mulder, NCAR, for Denver NWS rawinsonde data; C. Berg, NOAA/NESS for satellite photographs; and B. Hill, ARL/GMCC for secretarial expertise. In addition, the lead author gives thanks to the remaining GMCC staff, both past and present, for friendship plus the opportunity for professional and personal growth.

REFERENCES

Cadle, R. D., F. F. Fernald, and C. L. Frush, 1977. Combined use of lidar and numerical diffusion models to estimate the quantity and dispersion clouds in the stratosphere: Volcán de Fuego, 1974, and Augustine. J. Geophys. Res. 82:1783-1786.

Danielsen, E. F., 1981. Trajectories of the Mt. St. Helens eruption plume. Science 211:819-821.

Edlen, B., 1966. The refractive index of air. Metrologia 2:71-80.

Fegley, R. W., and H. T. Ellis, 1975. Lidar observations of a stratospheric dust cloud layer in the tropics. Geophys. Res. Lett. 2:139-141.

Fernald, F. G., and C. L. Frush, 1975. Lidar observations of the enhanced stratospheric dust layer associated with the eruption of Volcán de Fuego. Trans. Amer. Geophys. Union 56:366.

Fiocco, G., and G. Grams, 1964. Observations of the aerosol layer at 20 km by optical radar. J. Atmos. Sci. 21:323-324.

Fox, R. J., G. W. Grams, B. G. Schuster, and J. A. Weinman, 1973. Measurements of stratospheric aerosols by airborne laser radar. J. Geophys. Res. 70:7789-7801.

Fujiwara, M., T. Itabe, and M. Hirono, 1975. Sudden increase of stratospheric aerosol content after the eruption of Fuego volcano; lidar observations in Fukuoka. Report Ionosph. Space Res. Japan 29:74-78.

Grams, G., and G. Fiocco, 1967. Stratospheric aerosol layer during 1964 and 1965. J. Geophys. Res. 72:3523-3541.

Hofmann, D. J., and J. M. Rosen, 1981. On the background stratospheric aerosol layer. J. Atmos. Sci. 38:168-181.

Hofmann, D. J., J. M. Rosen, J. M. Kiernan, and J. Laby, 1976. Stratospheric aerosol measurements IV: global time variations of the aerosol burden and source considerations. J. Atmos. Sci. 33:1782-1788.

Hofmann, D. J., J. M. Rosen, T. J. Pepin, and R. G. Pinnik, 1975. Stratospheric aerosol measurements I: time variations at northern-midlatitudes. J. Atmos. Sci. 32:1446-1456.

Holton, J. R., 1972. An Introduction to Dynamic Meteorology. Academic Press, New York, New York.

Itabe, T., M. Fujiwara, and M. Hirono, 1977. Temporal variation of the stratospheric aerosol layer after the Fuego eruption observed by lidar in Fukuoka. J. Meteorol. Soc. Japan 55:606-611.

Iwasaka, Y., 1981. Variation of stratospheric aerosol content measured by laser radar; Part II, long term trend of post-Fuego eruption. J. Meteorol. Soc. Japan 59:446-451.

Jay, F. (ed.), 1977. IEEE Standard Dictionary of Electrical and Electronics Terms. Institute of Electrical and Electronics Engineers, Inc., New York, New York.

Junge, C. E., C. W. Chagnon, and J. E. Manson, 1961. Stratospheric aerosols. J. Meteorol. 18:81-108.

Kneizys, F. X., J. H. Chetwynd, Jr., R. W. Fenn, E. P. Shettle, L. W. Abreu, R. A. McClatchey, W. O. Gallery, J. E. A. Selby, 1980. Atmospheric transmittance/radiance: computer code lowtran 5. Report no. AFGL-TR-80-0067, Air Force Geophysics Laboratory, Hanscom A.F.B., Massachusetts.

Lenhard, R. W., 1973. A revised assessment of radiosonde accuracy. Bull. Amer. Meteorol. Sci. 54:691-693.

McCartney, E. J., 1976. Optics of the Atmosphere. Scattering by Molecules and Particles. John Wiley and Sons,Inc., New York, New York.

McCormick, M. P., T. J. Swissler, W. P. Chu, and W. H. Fuller, Jr., 1978. Post-volcanic stratospheric aerosol decay as measured by lidar. J. Atmos. Sci. 35:1296-1303.

Reiter, R., and W. Carnuth, 1975. Comparing lidar reflectivity profiles against measured profiles of vertical aerosol distribution between 1 and 3 km A.S.L. Arch. Met. Geophys. Biokl. Ser. A 24:69-92.

Reiter, R., H. Jäger, W. Carnuth, and W. Funk, 1979. The stratospheric aerosol layer observed by lidar since October, 1976. A contribution to the problem of hemispheric climate. Arch. Met. Geophys. Biokl. Ser. B 27:121-149.

Rosen, J. M., and D. J. Hofmann, 1980. A stratospheric aerosol increase. Geophys. Res. Lett. 7:669-672.

Russell, P. B., and R. D. Hake, Jr., 1977. The post-Fuego stratospheric aerosol: lidar measurements, with radiative and thermal implications. J. Atmos. Sci. 34:163-177.

Russell, P. B., W. Viezee, R. D. Hake, Jr., and R. T. H. Collis, 1976. Lidar observations of the stratospheric aerosol: California, October, 1972 to March, 1974. Quart. J. R. Met. Soc. 102:675-695.

Schuster, B. G., 1970. Detection of tropospheric and stratospheric aerosol layers by optical radar (lidar). J. Geophys. Res. 75:3123-3132.

Shortley, G., and D. Williams, 1971. Elements of Physics. Prentice-Hall, Inc., Englewood Cliffs, New Jersey.

Volz, F. E., 1975. Volcanic twilights from the Fuego eruption. Science 189:48-50.

APPENDIX:

Backscatter ratio, temperature, dewpoint, wind direction, and pressure data versus altitude above sea level and Boulder, Colorado.

5-19-80 to 7-29-80

The four axes labels are self explanatory. The thicker solid lines, beginning at 1 on the lower abscissas, are the backscatter ratio profiles; the thinner solid lines are the vertical temperature profiles. Moisture profiles are represented by thin dashed lines. The plotting models for winds are of standard World Meteorological Organization convention. Lidar and rawinsonde observation times are annotated in the upper right corner of each figure. Backscatter ratio peak values greater than 10.5 are listed next to dash marks on the backscatter ratio curves, at the peaks' corresponding altitudes.

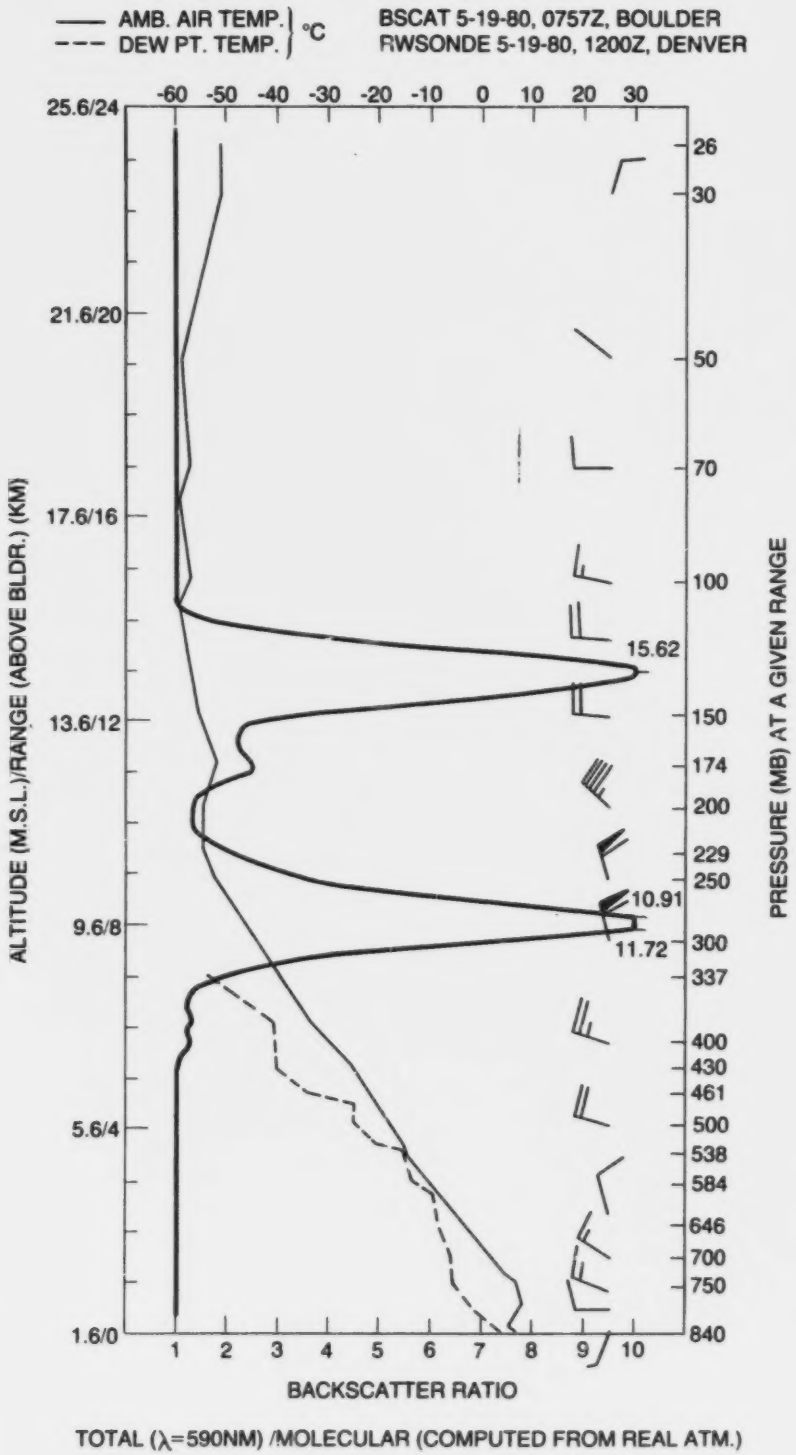

BEST DOCUMENT AVAILABLE

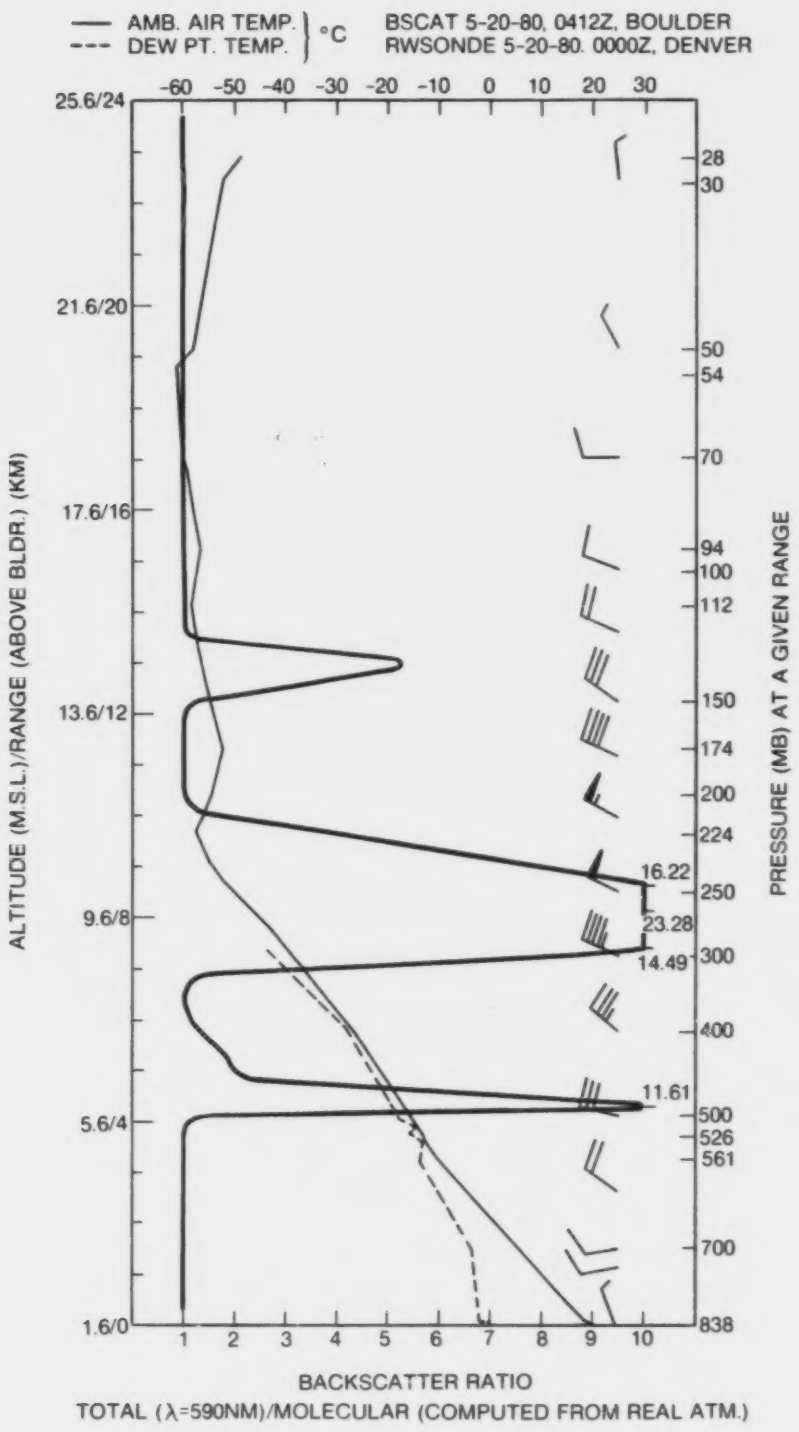

BEST DOCUMENT AVAILABLE

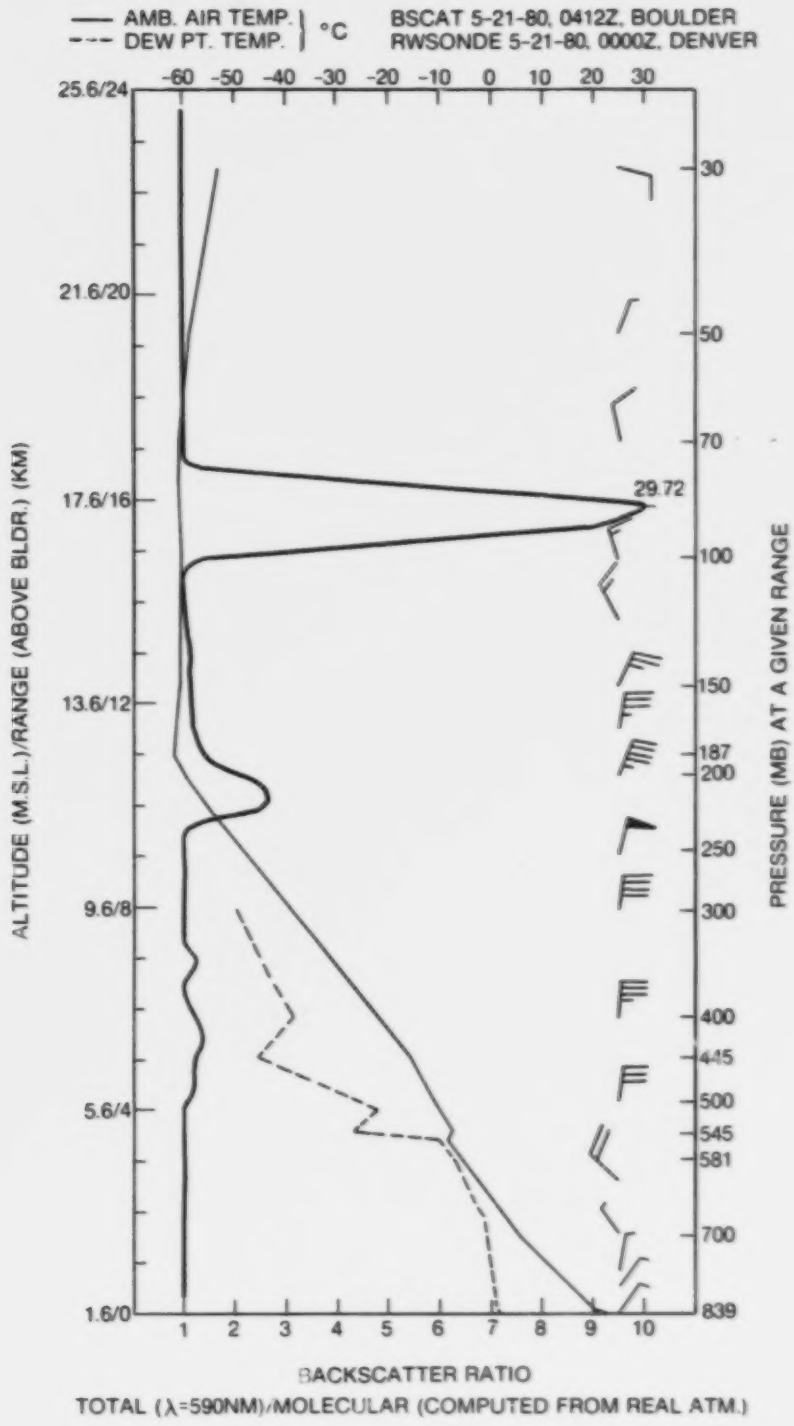

BEST DOCUMENT AVAILABLE

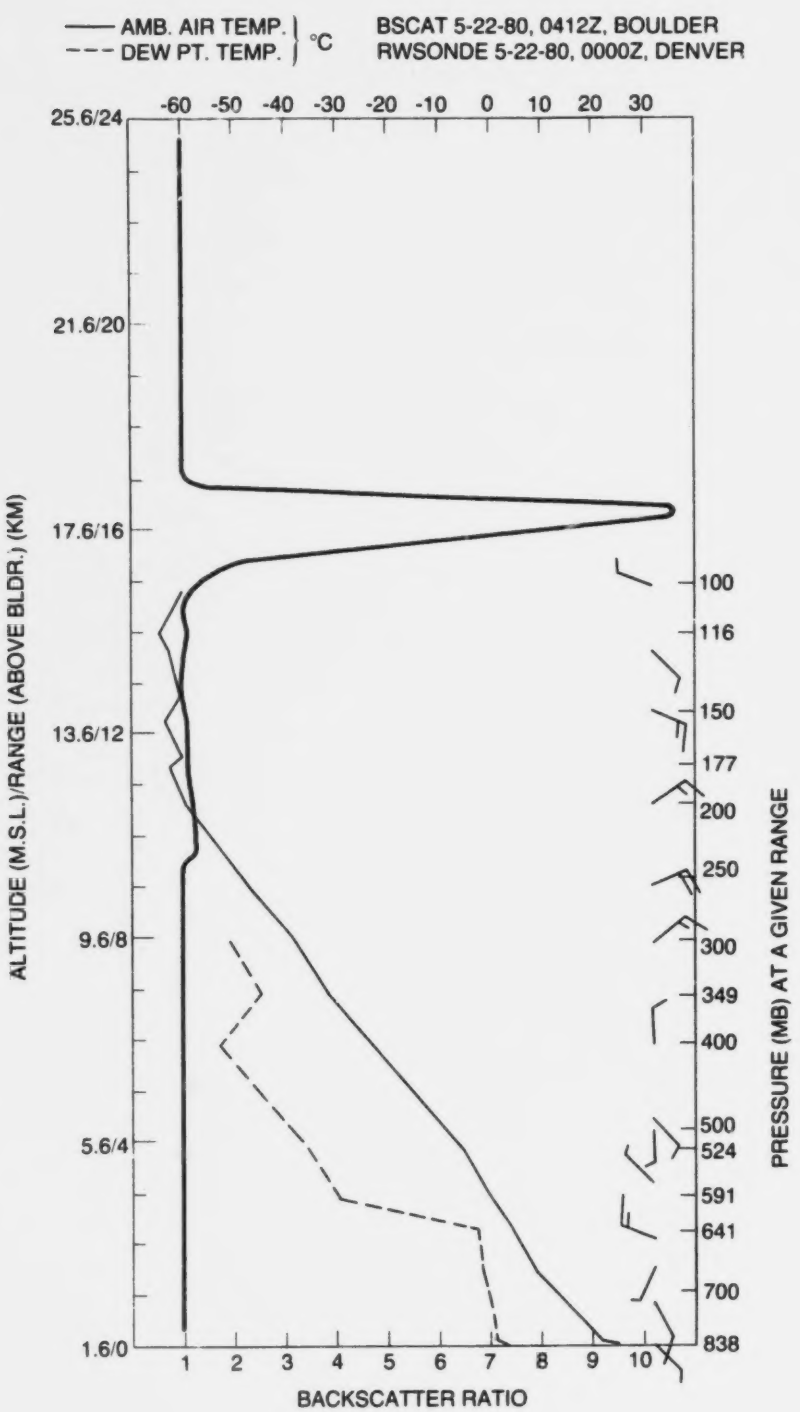

BEST DOCUMENT AVAILABLE

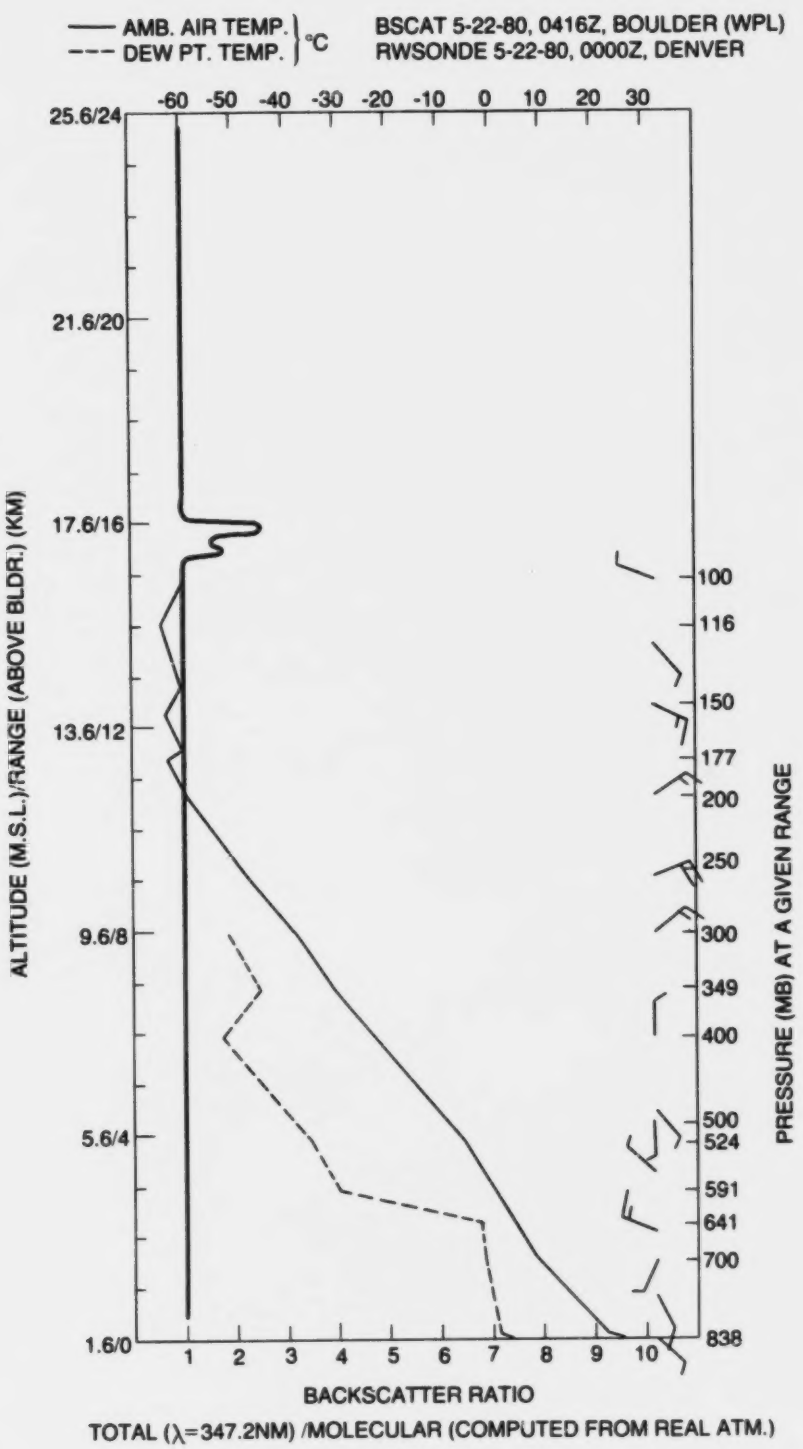

BEST DOCUMENT AVAILABLE

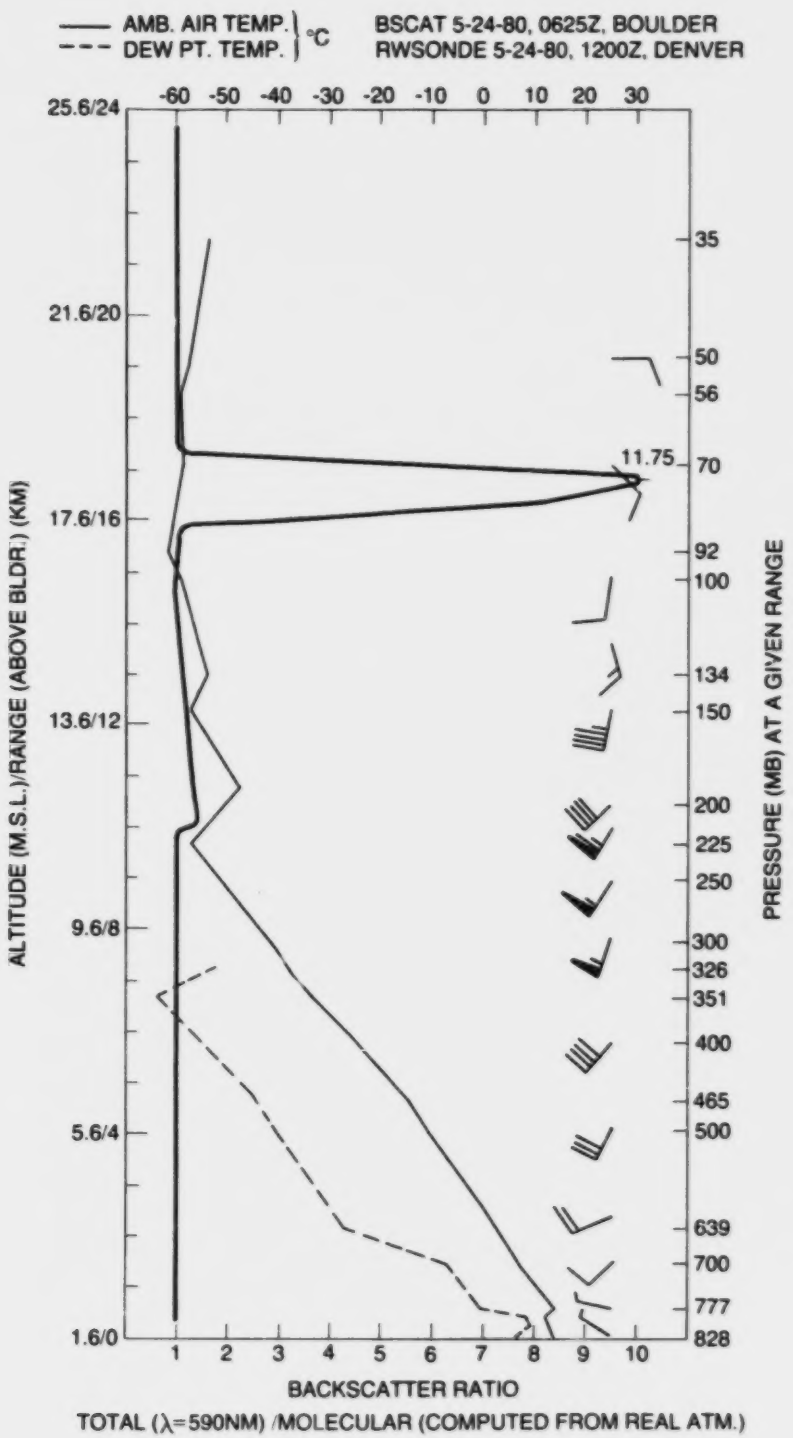

BEST DOCUMENT AVAILABLE

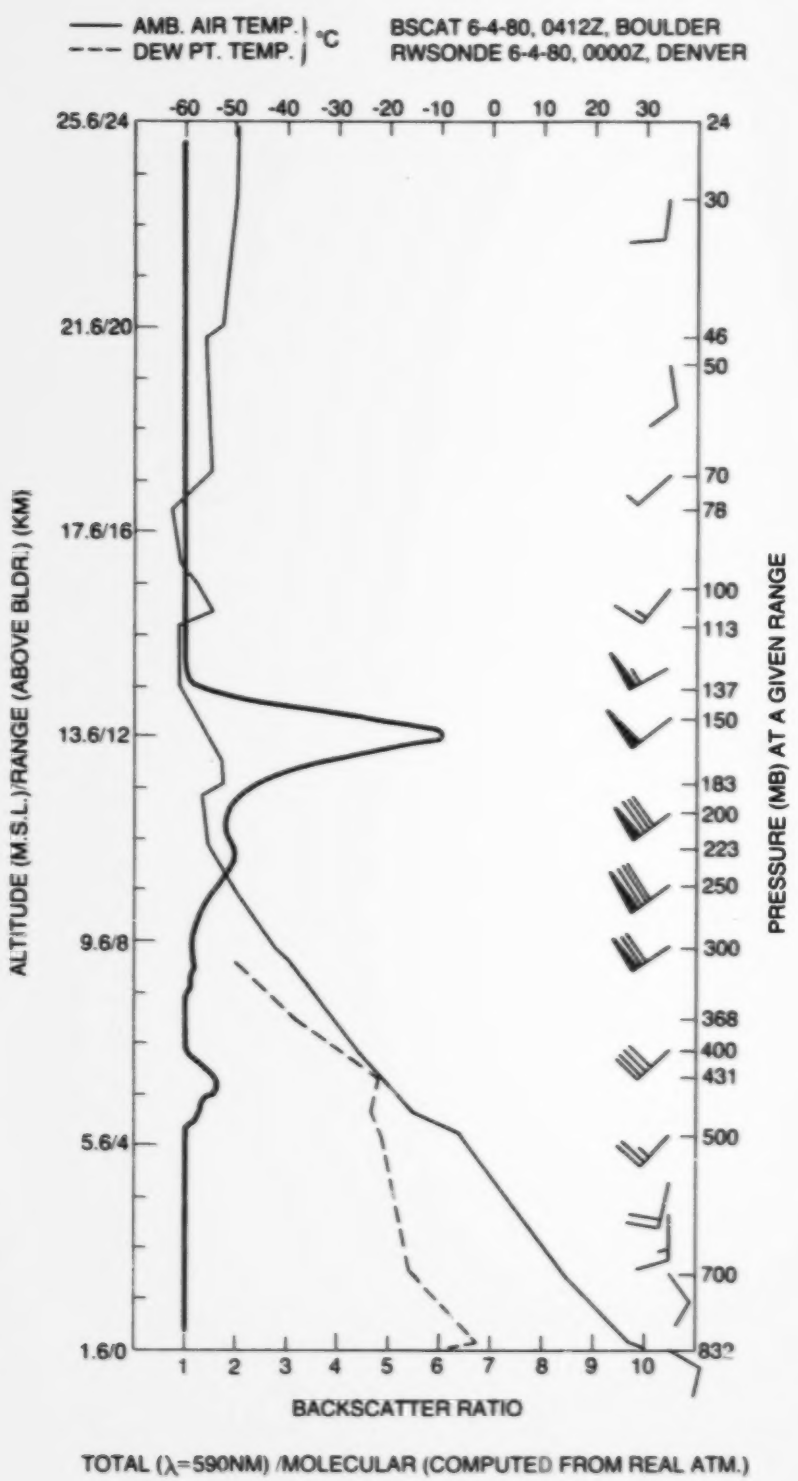

BEST DOCUMENT AVAILABLE

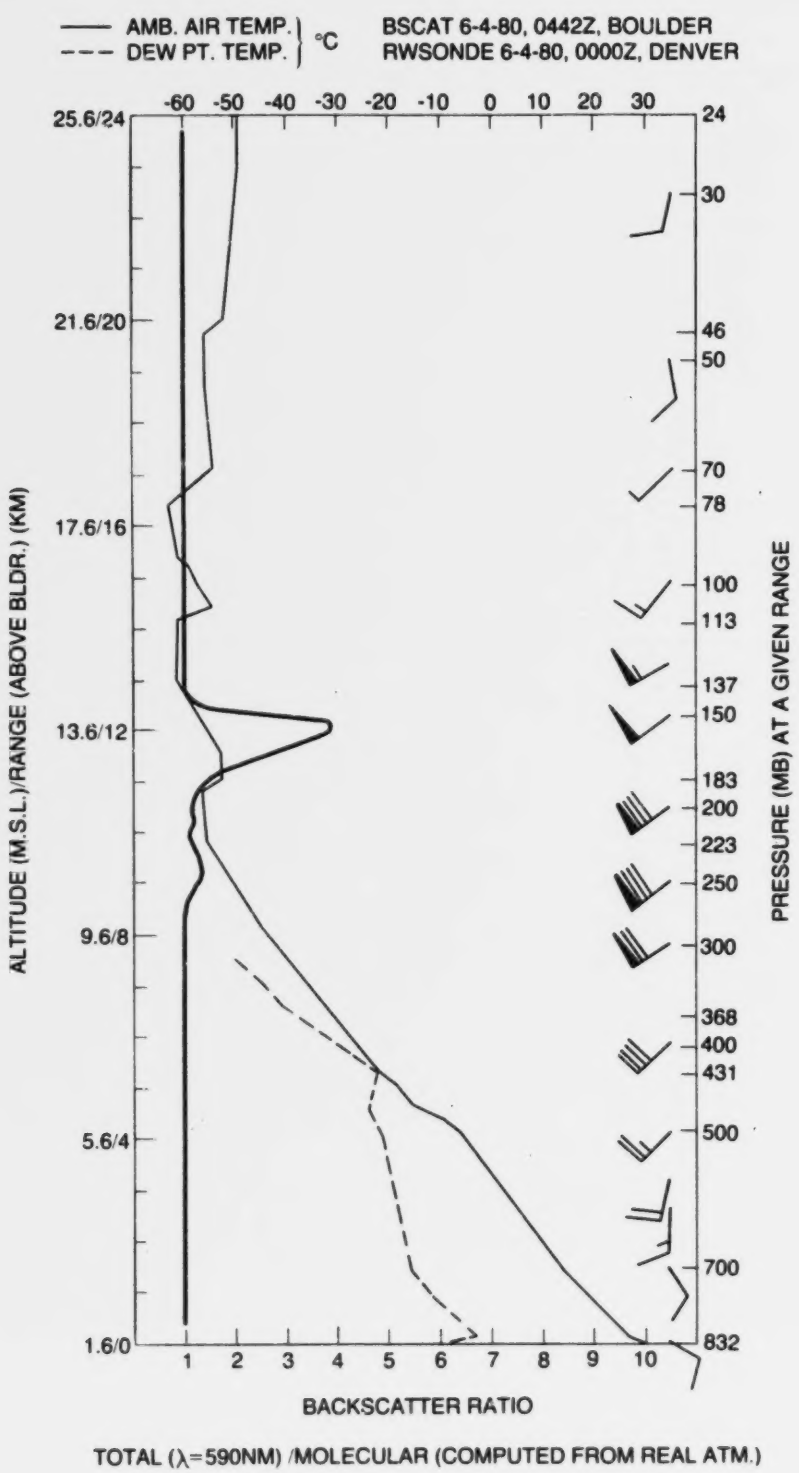

BEST DOCUMENT AVAILABLE

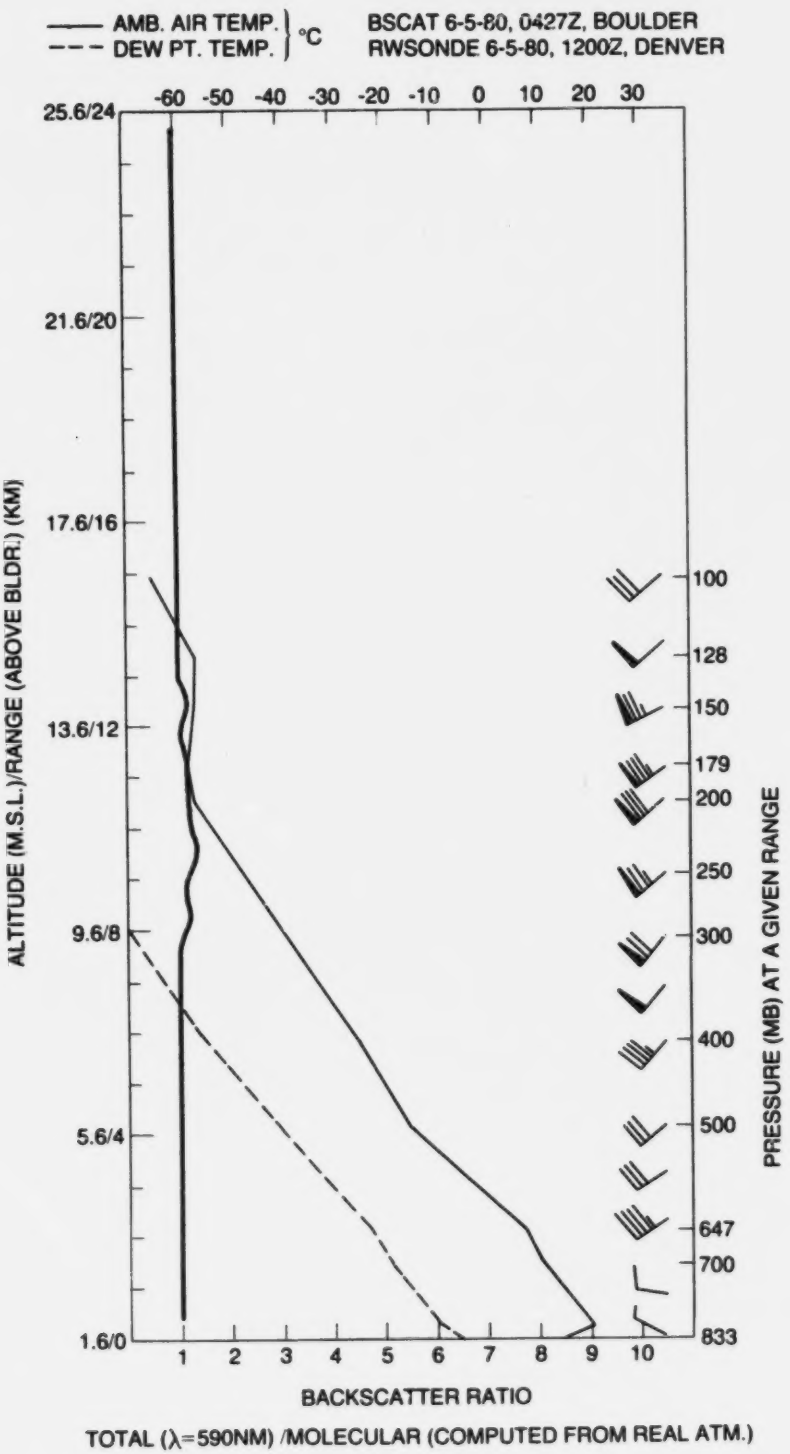

BEST DOCUMENT AVAILABLE

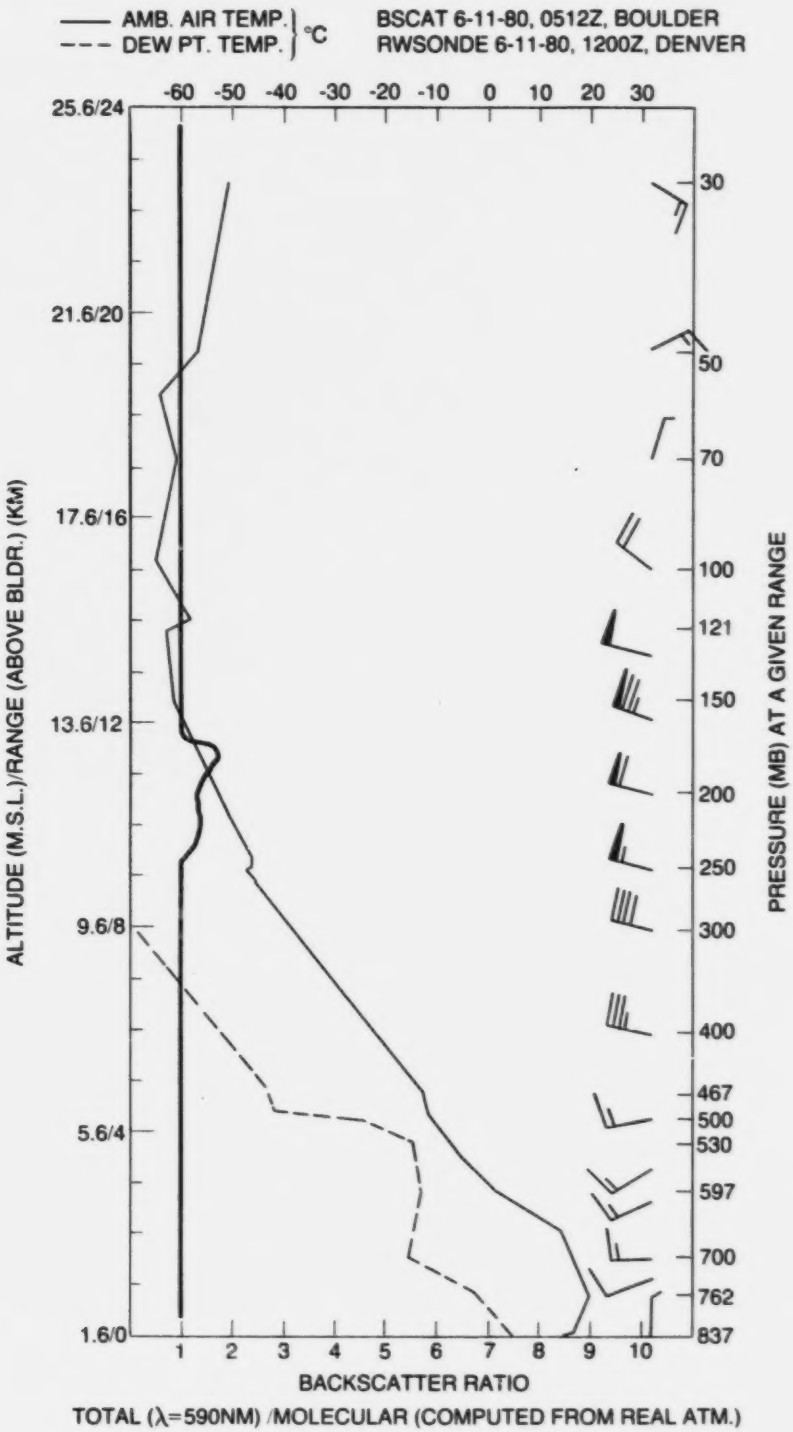

BEST DOCUMENT AVAILABLE

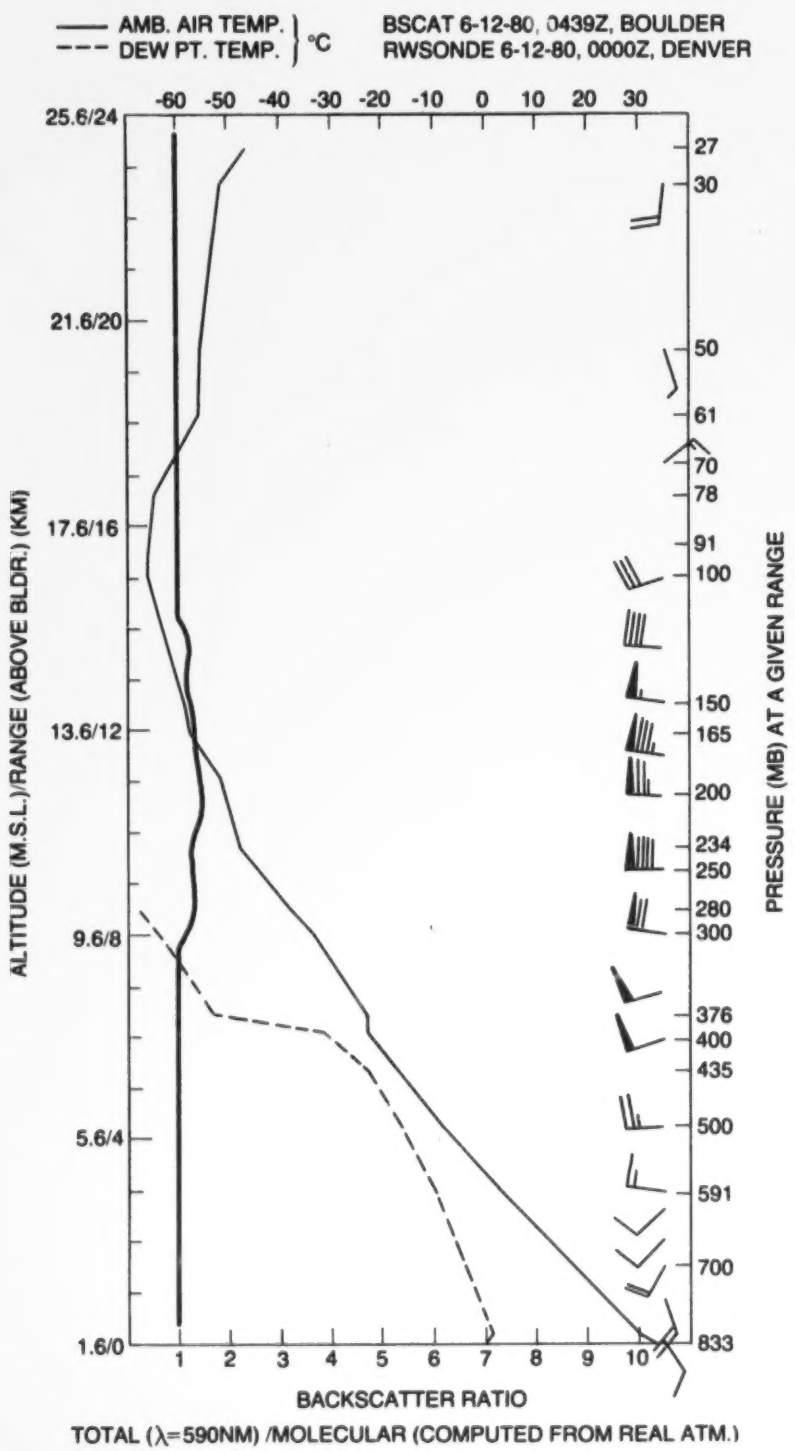

BEST DOCUMENT AVAILABLE

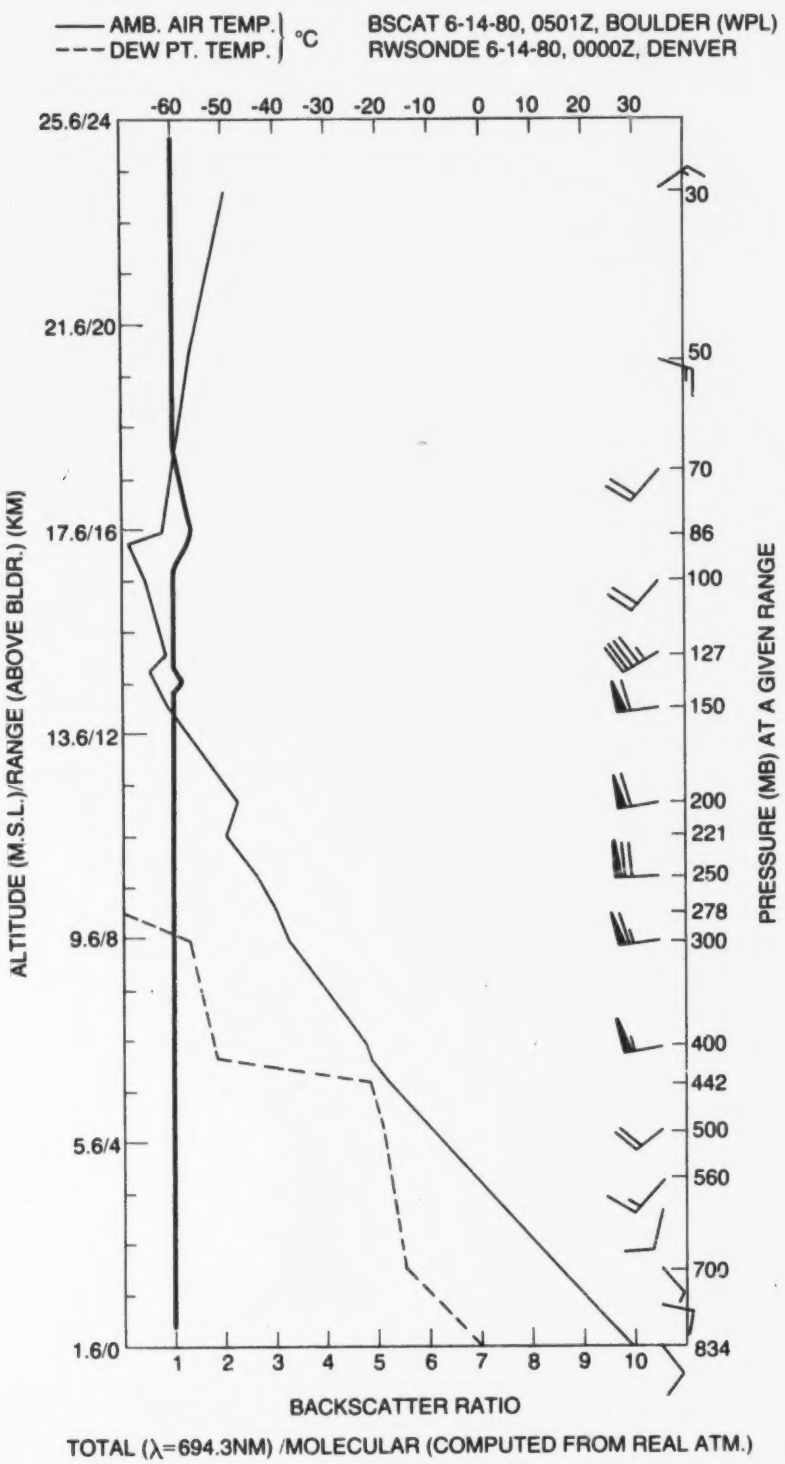

BEST DOCUMENT AVAILABLE

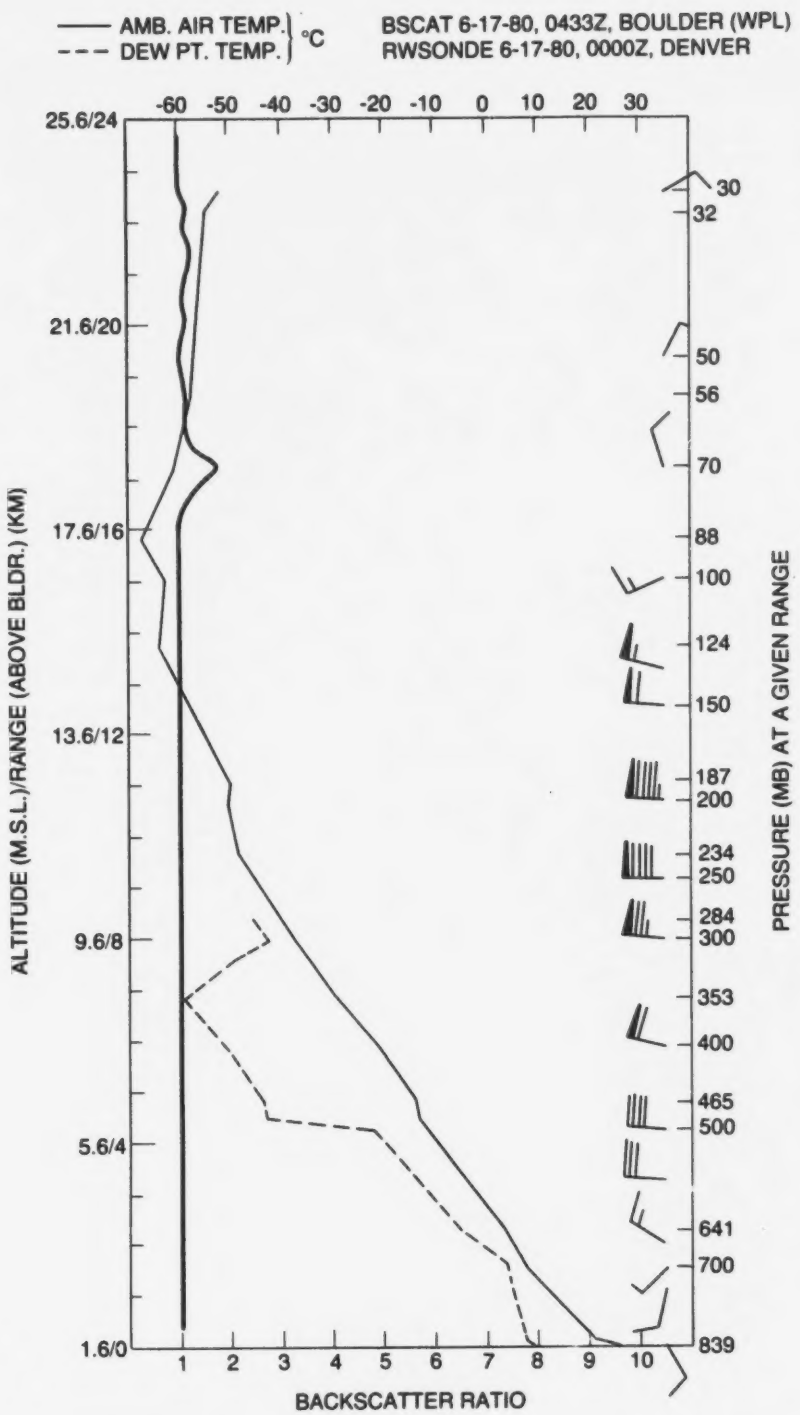

BEST DOCUMENT AVAILABLE

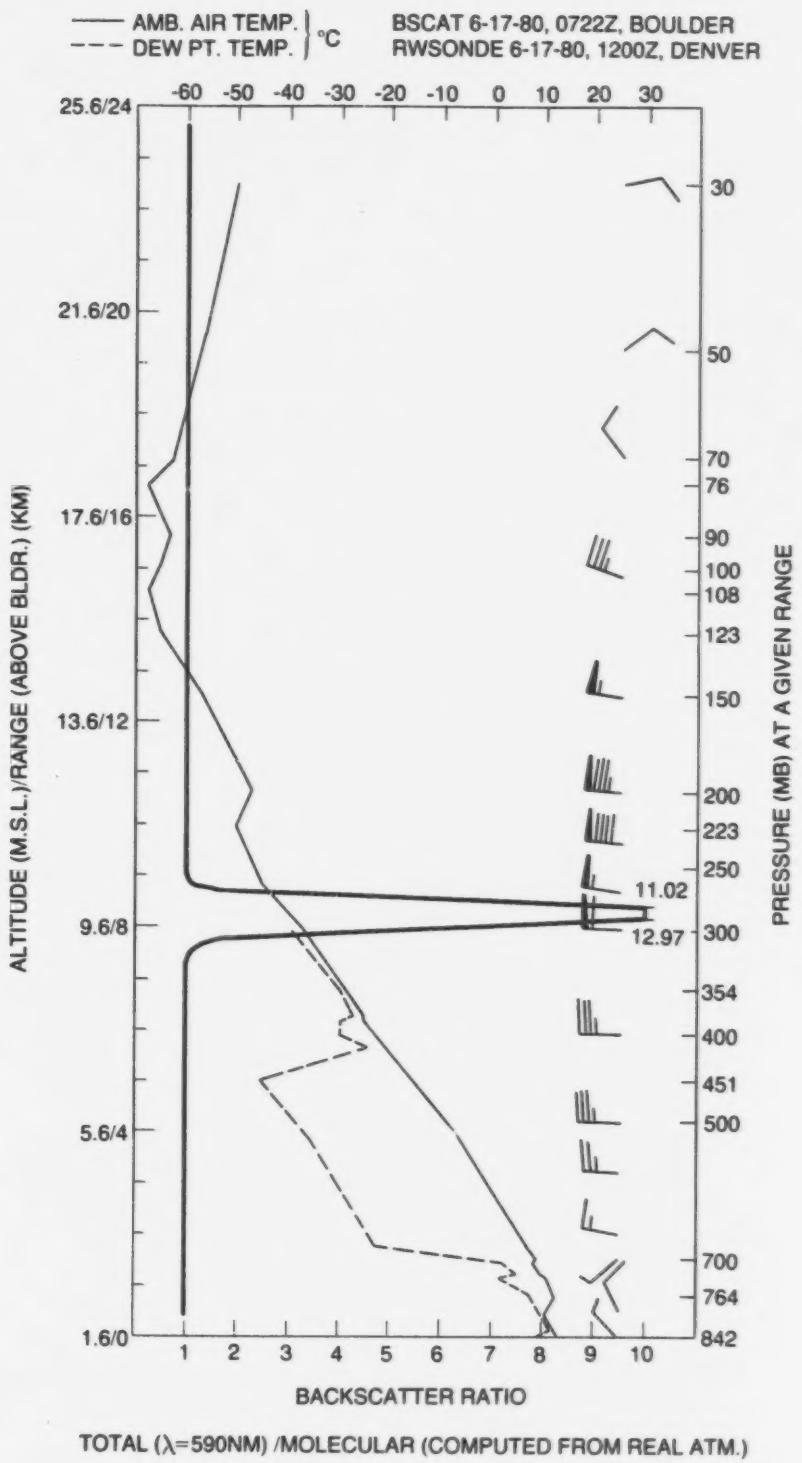

BEST DOCUMENT AVAILABLE

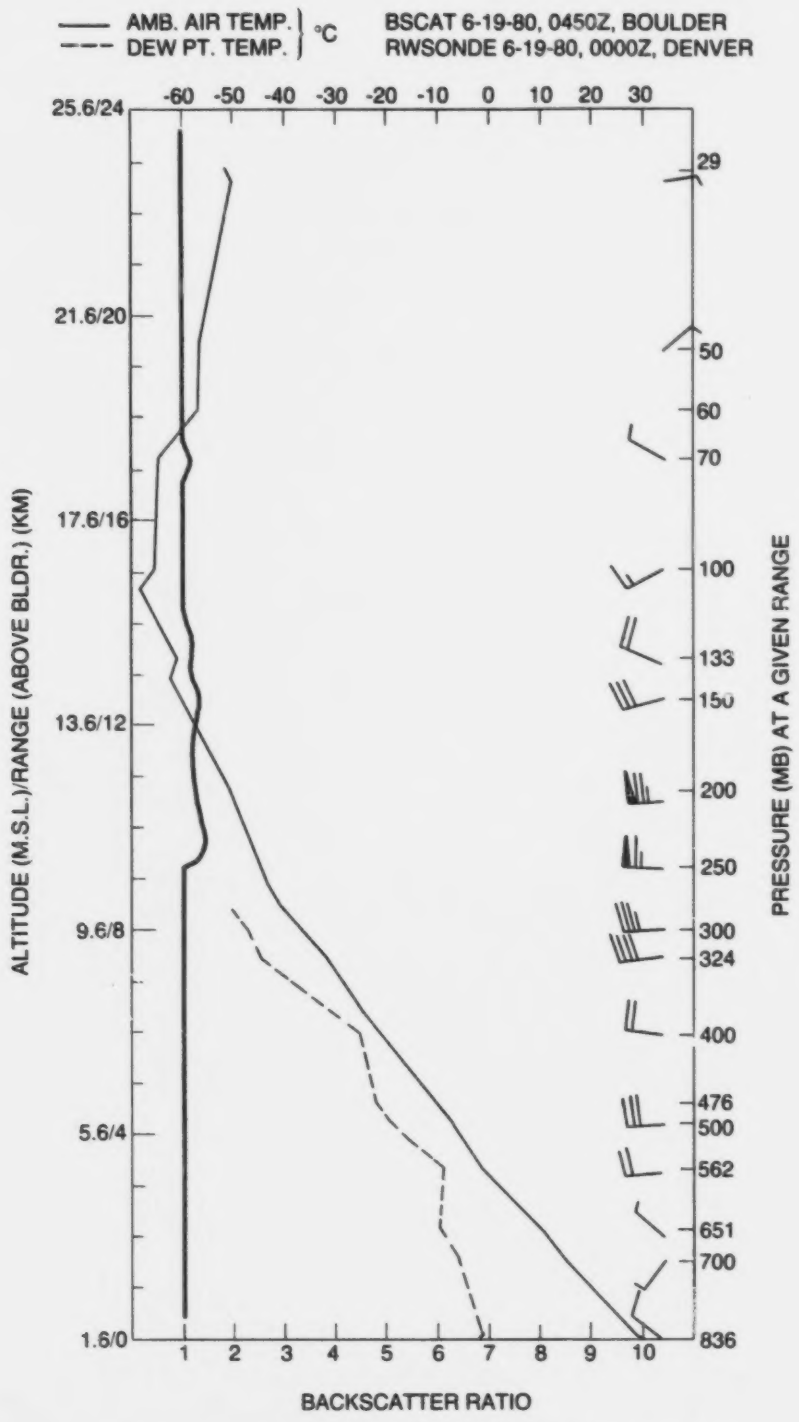

BEST DOCUMENT AVAILABLE

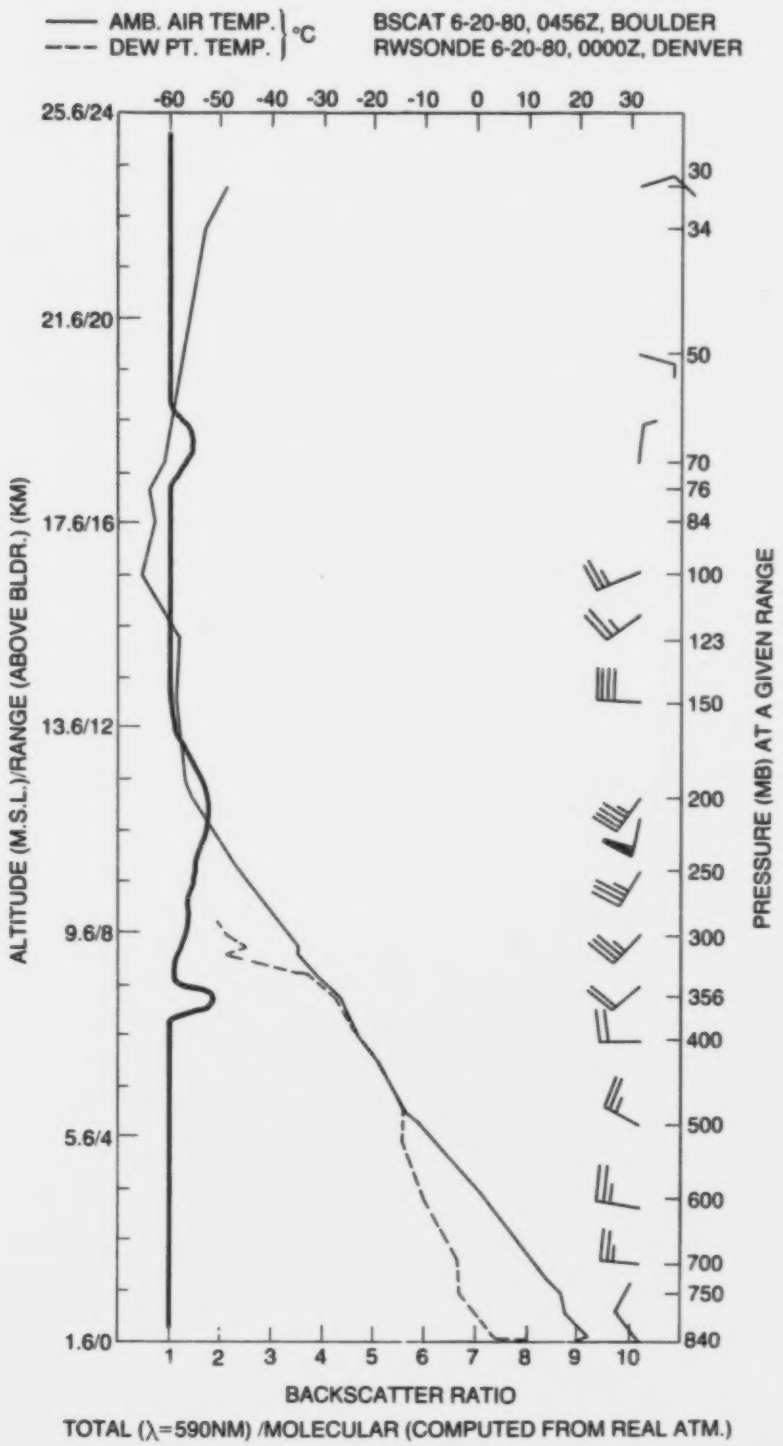

BEST DOCUMENT AVAILABLE

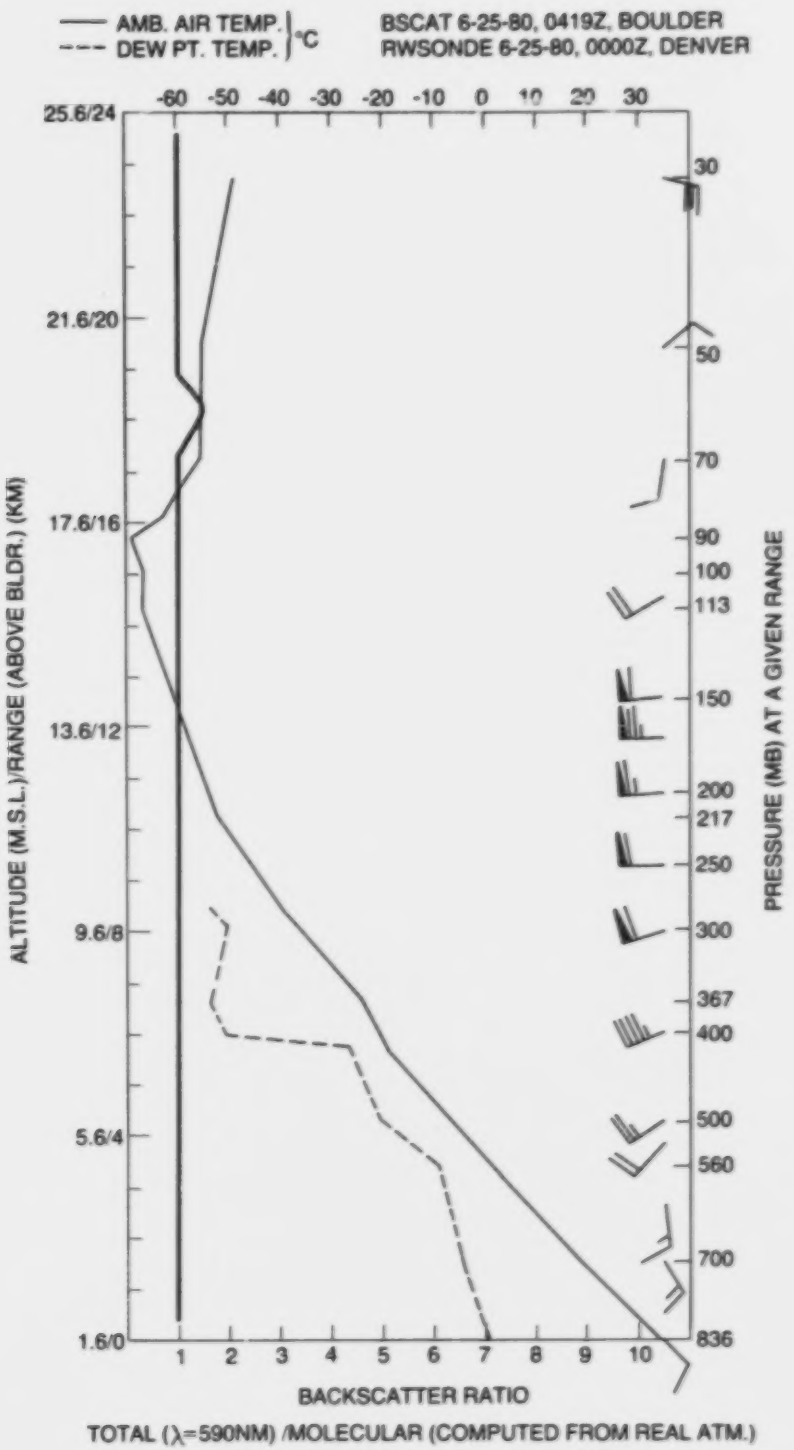

BEST DOCUMENT AVAILABLE

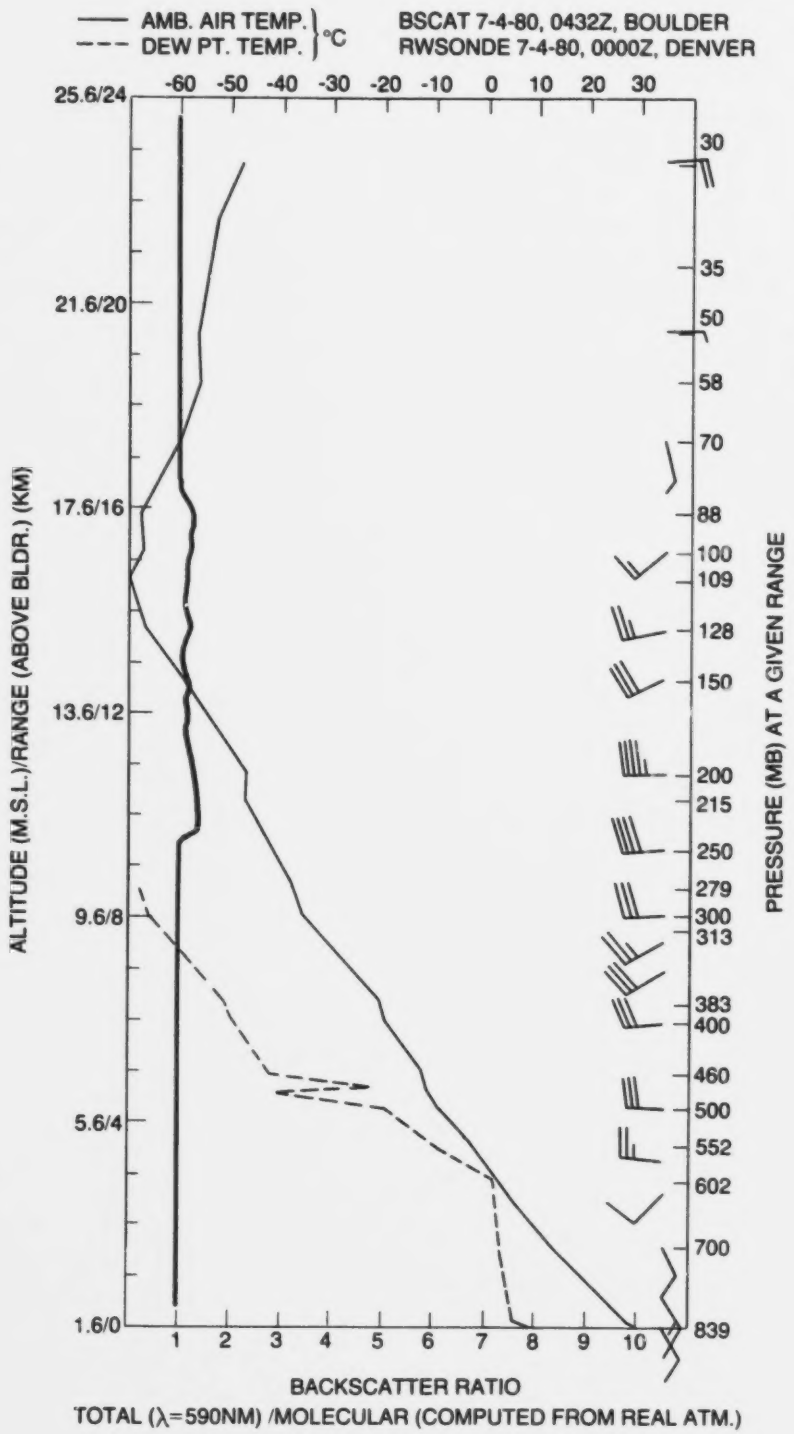

BEST DOCUMENT AVAILABLE

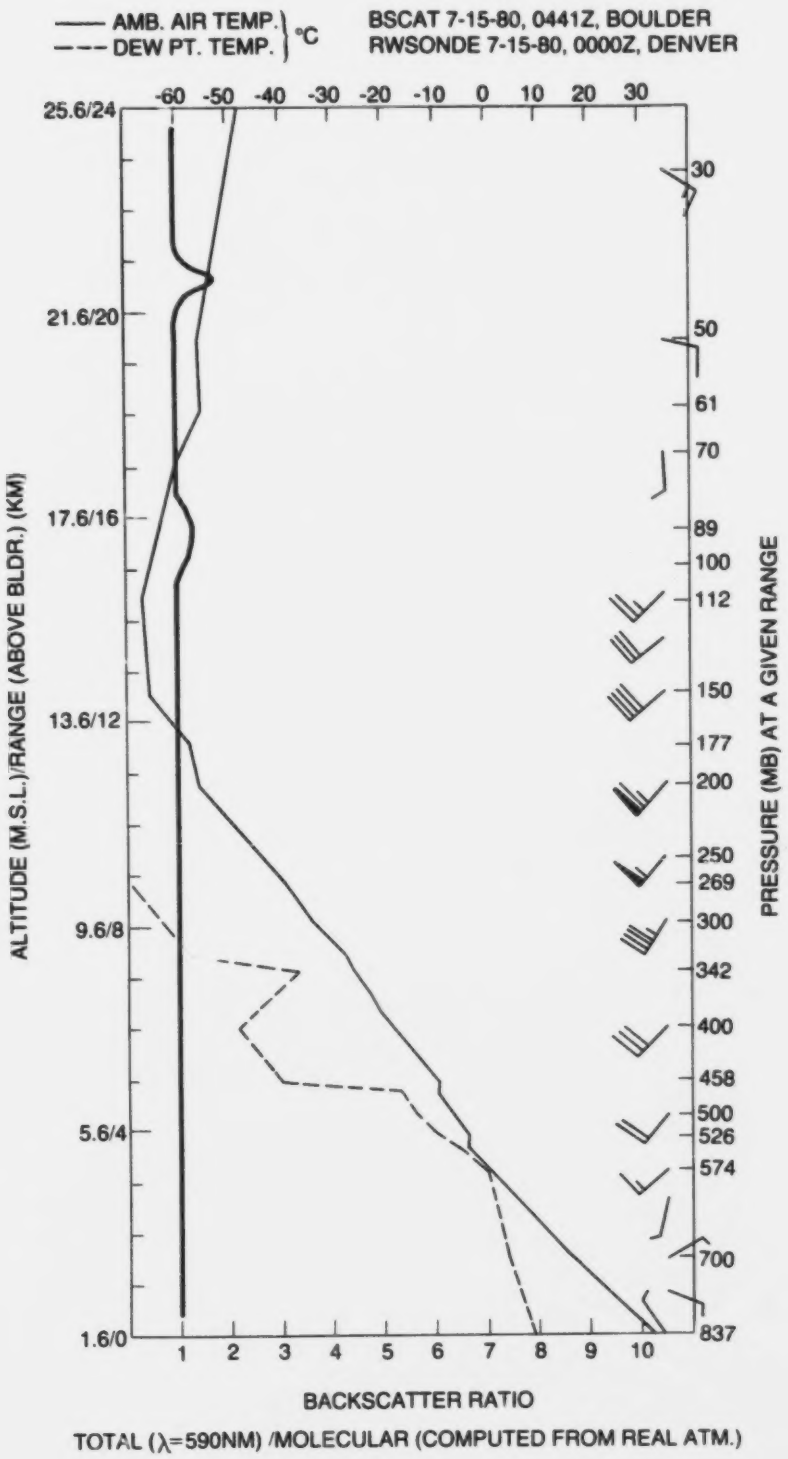

BEST DOCUMENT AVAILABLE

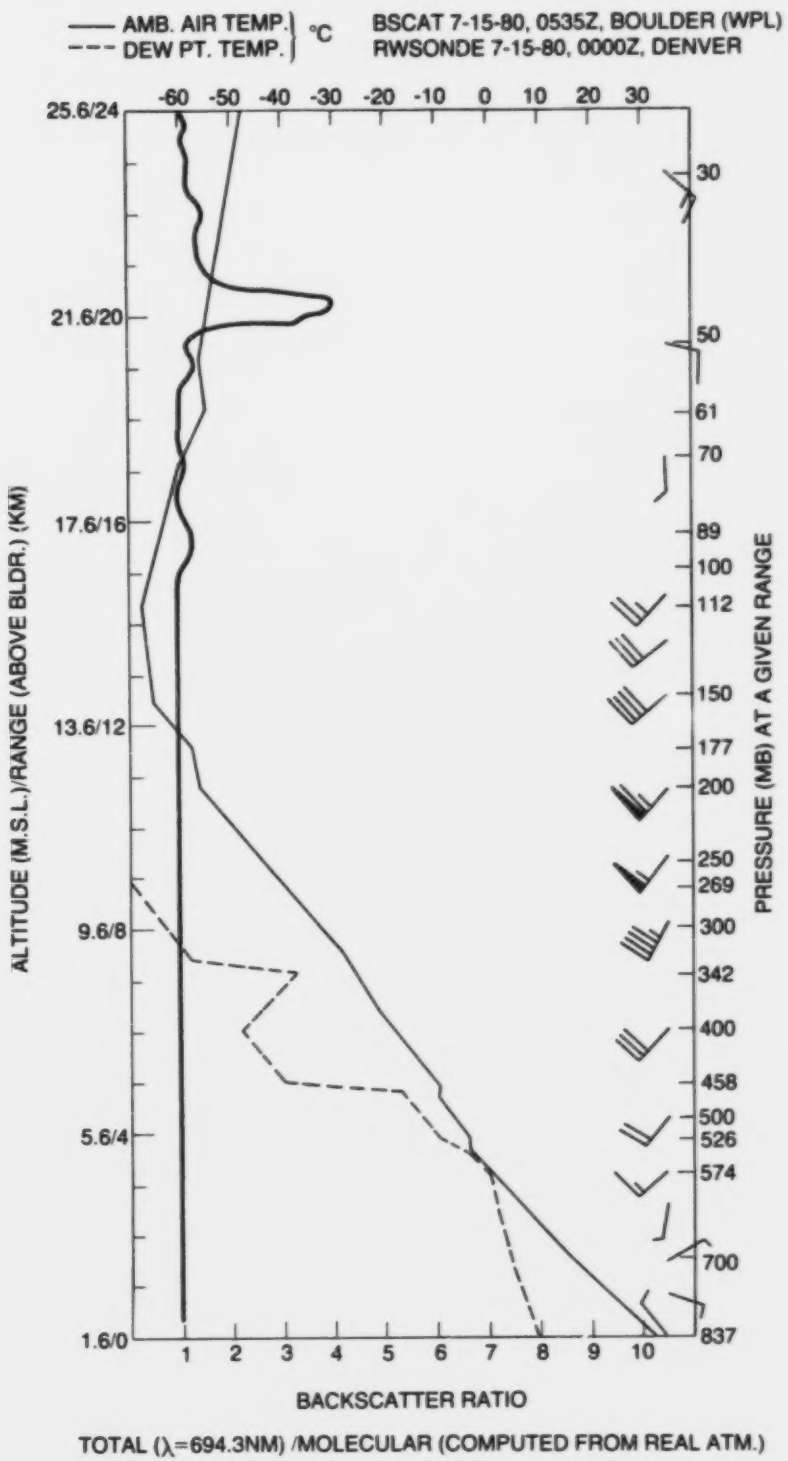

BEST DOCUMENT AVAILABLE

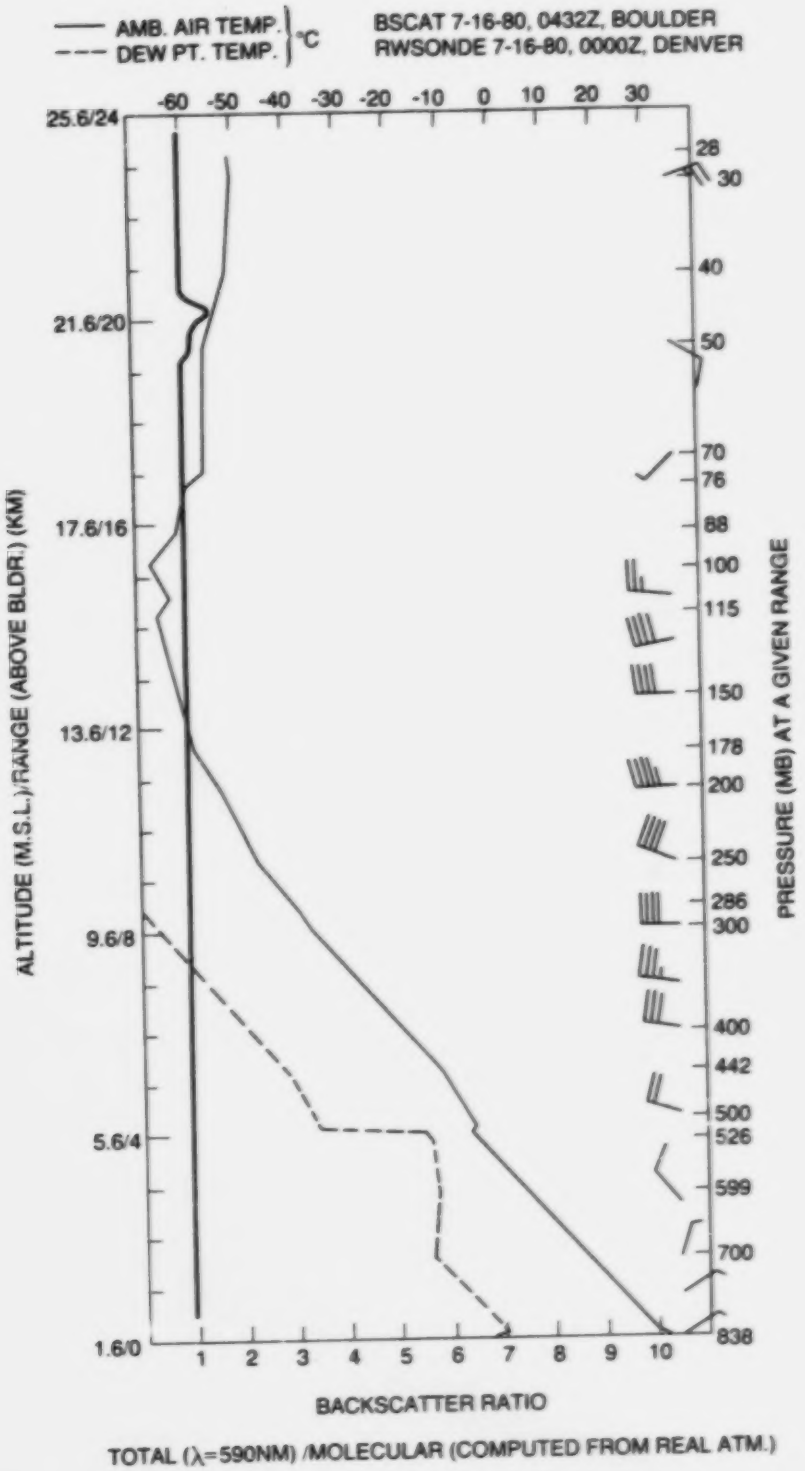

BEST DOCUMENT AVAILABLE

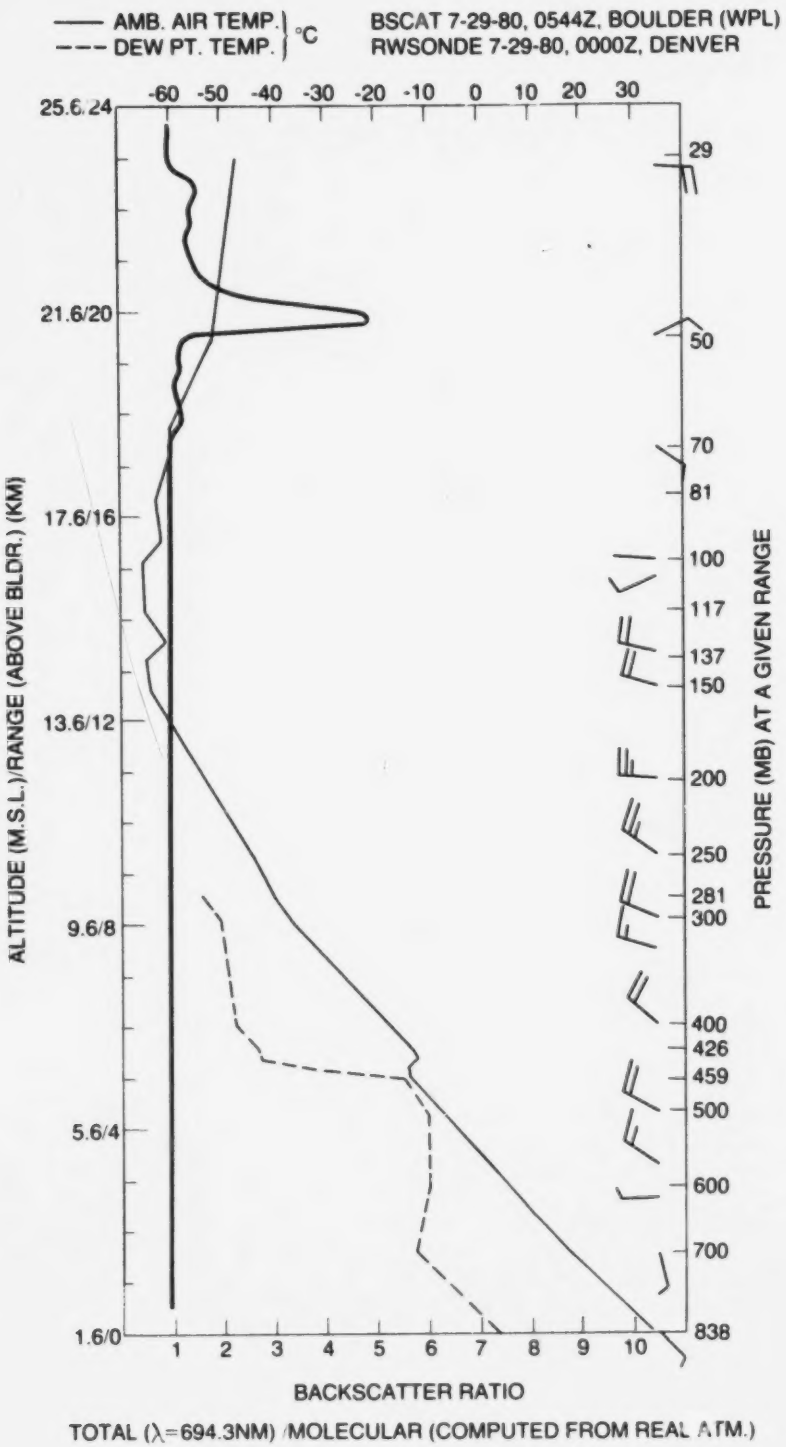

BEST DOCUMENT AVAILABLE